chemosensors

Review

Recent Advances in NIR-II Molecular Aggregates and Applications in the Biomedical Field

Kun Wu [1,†], Ruowen Yang [1,†], Xuefang Song [1], Huangxian Ju [1] and Ying Liu [1,2,*]

[1] State Key Laboratory of Analytical Chemistry for Life Science, School of Chemistry and Chemical Engineering, Nanjing University, Nanjing 210023, China; dg20240118@smail.nju.edu.cn (K.W.); 502023240125@smail.nju.edu.cn (R.Y.); 502022240094@smail.nju.edu.cn (X.S.); hxju@nju.edu.cn (H.J.)
[2] Chemistry and Biomedicine Innovation Center, Nanjing University, Nanjing 210023, China
* Correspondence: yingliu@nju.edu.cn
† These authors contributed equally to this work.

Abstract: Near-infrared (NIR) light is a promising tool for biomedical imaging and therapy, offering excellent tissue penetration, low scattering, and minimal biological fluorescence interference. An NIR-II optical range of 900–1880 nm with reduced background interference is particularly useful for disease diagnosis and treatment. Probes based on organic molecules are gaining attention for their structural flexibility and stable performance. Organic molecular aggregates, such as J-aggregates, H-aggregates, and aggregation-induced emission (AIE)-aggregates, exhibit unique optical properties like tunable spectral shifts, improved photostability, and higher absorption and fluorescence quantum yields. This mini review briefly discusses the advancements in NIR-II optical imaging and therapy technologies, focusing on the classification, formation mechanisms, and applications of organic molecular aggregates in disease diagnosis and treatment, offering a theoretical foundation and practical guidance for future research.

Keywords: NIR-II; molecular aggregates; J-aggregates; H-aggregates; aggregation-induced emission; imaging; therapy

Received: 31 December 2024
Revised: 6 February 2025
Accepted: 10 February 2025
Published: 13 February 2025

Citation: Wu, K.; Yang, R.; Song, X.; Ju, H.; Liu, Y. Recent Advances in NIR-II Molecular Aggregates and Applications in the Biomedical Field. *Chemosensors* **2025**, *13*, 67. https://doi.org/10.3390/chemosensors13020067

1. Introduction

Near-infrared (NIR) light, due to its excellent tissue penetration, low light scattering, and minimal biological fluorescence background interference, has emerged as a cutting-edge technology in biomedical imaging and therapy, offering new possibilities for early disease diagnosis and precision treatment [1–6]. The NIR-II range of 900–1880 nm wavelength features superior tissue penetration depth, low light scattering, and reduced biological fluorescence background, making it a leading technology in the field of biomedical imaging and therapy [7–9]. Fluorescence probes in the NIR-II range are gaining increased attention due to their excellent biocompatibility, degradability, and flexibility in structural design [10].

Organic molecular aggregates, as a key component of NIR-II materials, have become an important research direction in the field due to their unique advantages in imaging and disease treatment [11–13]. Compared to monomers, organic molecular aggregates typically exhibit distinctive optical properties, such as tunable spectral changes, enhanced photostability, stronger light absorption, and higher fluorescence quantum yields. These advantages make them more competitive in biomedical applications, particularly in complex biological environments, where their performance far exceeds that of monomeric forms [14–16]. Depending on the nature of intermolecular interactions, organic molecular aggregates can

be classified into J-aggregates [17], H-aggregates [18], and AIE-aggregates [19], among others [20].

J-aggregates exhibit significant spectral redshift due to molecular sliding arrangements, enabling absorption and emission at longer wavelengths, which is ideal for deep-tissue imaging [21,22]. However, in tightly packed J-aggregates, notable charge-transfer phenomena may occur, which, while enhancing the spectral redshift, could also lead to fluorescence quenching. Despite this, J-aggregates demonstrate excellent performance in light absorption and photothermal conversion, showing great potential for applications in photoacoustic imaging (PAI) and photothermal therapy (PTT) [23–26]. H-aggregates, due to aggregation-induced fluorescence quenching effects, can significantly enhance thermal conversion and acoustic signals, which show more advantages in PA imaging and PTT [27–30]. Recent studies have shown that some H-aggregates possess a unique anti-Kasha emission mechanism, which, under certain conditions, can produce rare fluorescence emissions [31–34]. With proper design, this special luminescent phenomenon can be used for specific imaging and therapeutic functions in complex biological environments. Aggregation-induced emission (AIE)-aggregates have attracted considerable attention for their enhanced emission in the aggregated state. Unlike traditional fluorescent molecules, which experience fluorescence quenching in aggregate form, AIE molecules can significantly boost fluorescence signals at high concentrations or in aggregates [35,36].

Their advantage in disease imaging lies in the ability to significantly increase the signal intensity, demonstrating high sensitivity for low-concentration targets. Furthermore, AIE materials can efficiently generate reactive oxygen species in photodynamic therapy, offering strong tumor cell-killing capability and providing robust support for integrated imaging and therapy applications [37].

This mini review systematically outlines the research background of NIR-II optical imaging and therapy technologies and their significant applications in disease diagnosis and treatment. It provides a detailed analysis of the core characteristics of NIR-II optical materials, with a focus on the classification, formation mechanisms, and practical applications of organic molecular aggregates in disease diagnosis and treatment (Figure 1). The review lays a theoretical foundation and provides practical guidance for future research.

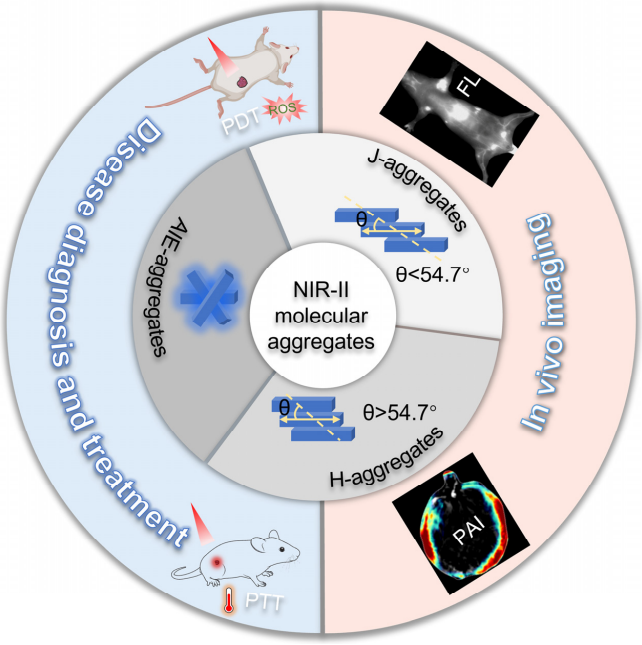

Figure 1. Schematic illustration of the main types of NIR-II molecular aggregates and their applications in the biomedical field.

2. NIR-II Molecular Aggregates

Organic molecular probes offer significant advantages in terms of enhanced biocompatibility, pharmacokinetics, and targeting capability, which are beneficial for approval by the U.S. Food and Drug Administration (FDA) and clinical translation. However, they generally suffer from lower luminescence efficiency, poorer photostability, and relatively shorter emission wavelengths. To overcome these limitations, researchers have developed a range of specially structured molecules and imaging enhancement strategies. Currently, the organic probes used for NIR-II window imaging and therapy mainly include polymeric materials [38] and organic small-molecule dyes. Among these, organic small-molecule dyes can be further categorized into donor–acceptor (D-A) and donor–acceptor–donor (D-A-D) charge-transfer dyes based on diketopyrrolopyrrole (DPP), isoindigo (IID), triazole [4,5-g]-quinoxaline (TQ), and benzobisthiazole (BBTD) [39]. Additionally, polymethine skeleton [40], rhodamine [41], and boron dipyrromethene (BODIPY) structures [42] as the central cores have also been explored. Some dyes with NIR-I peak emissions, such as indocyanine green (ICG) and IRDye 800CW, have successfully been applied to the NIR-II imaging field due to the tailing of their emission spectra into the NIR-II range [43–45]. In addition to free organic compounds, their aggregates, including J-aggregates, H-aggregates, and AIE-aggregates, have also garnered attention in disease diagnosis and therapy [22,46,47].

2.1. J-Aggregates

J-aggregates are known for their unique optical properties, which include significant redshifts in both absorption and emission spectra compared to monomers, extremely narrow bandwidths, exciton delocalization, and efficient energy-transfer capabilities. These characteristics have led to their widespread applications in spectroscopy, optoelectronic devices, and bioimaging. As early as 1936, Jelley observed an anomalous redshift in the absorption and emission spectra of 1,1′-diethyl-2,2′-cyano (PIC) molecules in aqueous solution [48]. In the same year, Scheibe also observed similar phenomena [49]. Compared to the spectra in organic solvents (such as ethanol), the absorption peak of PIC in water undergoes a significant redshift when its concentration exceeds 10^{-3} M. As the concentration increases further to 10^{-2} M, the absorption peak becomes stronger and sharper, with a noticeable deviation from Beer's law [50] (Figure 2A). Additionally, adding sodium chloride to the PIC aqueous solution induces similar spectral changes, with sharper peaks, a full width at half maximum (FWHM) of about 200 cm^{-1}, and a higher molar absorption coefficient (ε). Fluorescence emission also increases but with a minimal Stoke's shift. Scheibe believed this was the result of desolvation during the aggregation process of the molecules, with the changes in the absorption spectra originating from the "neighbor effect" between adjacent molecules. Jelley, on the other hand, observed that when nonpolar solvents or 5 M sodium chloride solution were added to the ethanol solution, PIC would rapidly precipitate, and as the dye crystallized, its fluorescence disappeared. This might have led Jelley to mistakenly attribute the spectral changes to individual dye molecules rather than their aggregates [51]. In recent years, J-aggregates (or Scheibe aggregates) generally refer to dye molecular aggregates with narrow redshifted absorption bands and small Stoke's shift fluorescence [52,53].

With the continuous advancement of research, Kasha et al. (1965) [54] established a connection between the packing arrangement of molecular aggregates and their photophysical properties based on long-range Coulomb coupling. Building on the Frenkel exciton (FE) theory, they proposed the molecular aggregate exciton model [55], which provided a theoretical foundation for explaining the optical behavior of J-aggregates. Taking a dimer with an inclined stacking arrangement as an example, the exciton model describes its energy level structure and exciton state splitting energy ($\Delta\varepsilon$), as shown in Figure 2B. Here,

M represents the transition dipole moment of the original exciton state, d_{c-c} denotes the intermolecular center-to-center distance within the dimer, and θ is the slip angle of the dimer. The angle θ between the transition dipole and the molecular axis of the aggregate determines whether the transition will lead to a lower or higher excitation energy level. When the slip angle θ is smaller than the critical value of 54.7°, the splitting of the original singlet exciton state can generate a low-energy exciton state with a larger transition dipole moment (J-aggregate), causing the maximum absorption wavelength of the aggregate to redshift relative to the monomer. Conversely, when θ exceeds the critical value of 54.7°, the transition allows for excitation into a higher energy state, forming an H-aggregate, which results in a blue-shift in absorption [56] (Figure 2B).

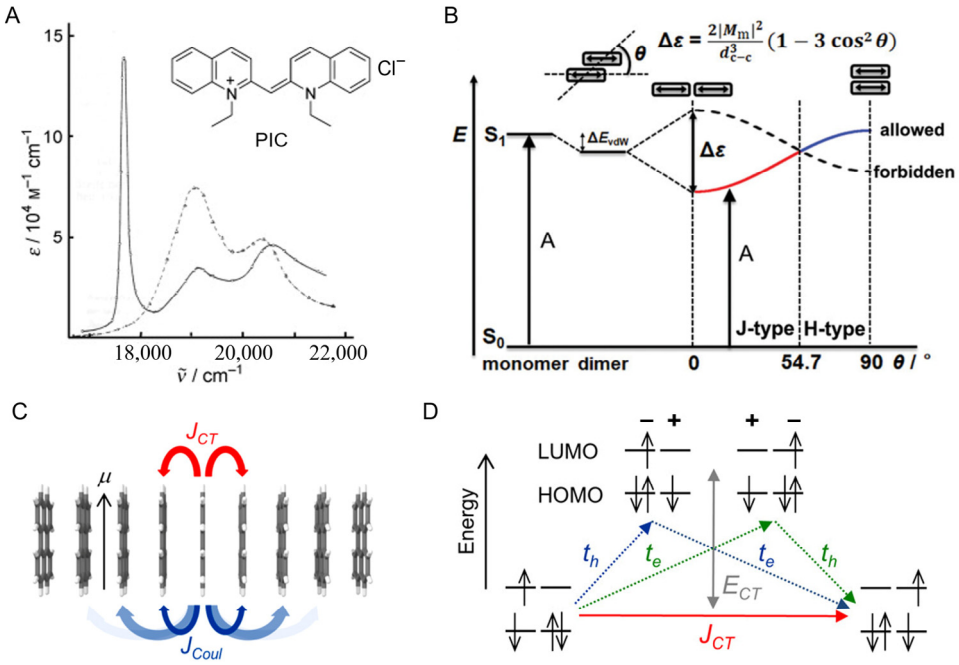

Figure 2. (**A**) Absorption spectra of PIC aggregates in water (solid line) and its monomers in ethanol (dot line). (**B**) A schematic illustration for an energy diagram of aggregated dimers (represented by gray rectangles) with coplanar transition dipoles inclined to the interconnected axis by angle θ. Double arrows represent the polarization axis for the molecular electronic transition considered. A = absorption; ΔE_{vdW} = difference in van der Waals interaction energies between ground and excited states. (**C**) Model perylene π-stack showing short-range charge-transfer (CT)-mediated interactions, J_{CT}, and long-range Coulomb interactions, for which J_{Coul} is the nearest neighbor. (**D**) Energy level diagram depicting a charge transfer between neighboring chromophores. J_{CT} results from the sum of the blue and green virtual two-step pathways. The images are reproduced with permission from [56–58].

Compared to the redshift of the absorption spectrum of monomers or the presence of slip-stacked arrangements in aggregates, these phenomena alone are not sufficient to classify an aggregate as a J-aggregate. However, in recent years, the definition of J-aggregates has been progressively expanded [59]. In the decades following the pioneering work of Jelley and Scheibe, although the fluorescence properties of some dyes did not fully conform to the classical definition of J-aggregates and did not exhibit the characteristic narrowing of the absorption band, they have still been broadly categorized as J-aggregates. In classical J-aggregates, the low exciton state energy levels, generated by the long-range Coulomb coupling (J_{Coul}) mechanism, are the allowed transition levels (Figure 2B,C). This J_{Coul} coupling mechanism leads to the typical features of classical J-aggregates: a narrowed absorption spectrum, an increased molar absorptivity, a pronounced redshift,

and a reduction in the fine vibrational structure of the monomer. Similarly, the fluorescence spectrum narrows, the Stoke's shift is small, the fluorescence lifetime is shorter, and the fluorescence quantum yield is higher [59].

Although the molecular aggregate exciton theory based on Kasha's framework explains many examples of H-aggregates and J-aggregates, there are still some "non-conventional" aggregates that cannot be fully understood within this theoretical framework [58]. For example, a redshift in absorption does not necessarily originate from the long-range Coulomb coupling (J_{Coul}) mechanism; it may also result from a short-range charge-transfer (CT)-mediated coupling mechanism (J_{CT}) (Figure 2C). This coupling mechanism primarily occurs when molecules are in close proximity to one another (typically less than 5 Å, especially around 3.5 Å for π–π stacking distances), a geometric configuration that allows for charge transfer or wavefunction overlap between adjacent molecules (wavefunction overlap is a short-range exchange interaction). As shown in Figure 2C, short-range interactions (Dexter [60], or exchange interactions arising from wavefunction overlap) can be intuitively understood within a simple model based on disordered linear π-stacking. This model contains *N* chromophores, with one molecule in each unit cell [58,61]. Each molecule has an electronic transition from S_0 to S_1 (HOMO-LUMO), with an energy E_{S1} and a transition dipole moment μ, both of which are independent of the molecule's position within the stack.

Unlike J_{Coul}, J_{CT} can convert a local excitation state (LE) into a charge-transfer state (CT). The CT state typically has lower energy, where an electron moves from one molecule to a neighboring molecule, and a hole is left on the original molecule from which the electron was transferred [58] (Figure 2D). The dissociation of the electron and hole can be described by the intermolecular transfer integrals, denoted as t_e (electron transfer ability, which depends on the overlap of the lowest unoccupied molecular orbital (LUMO) between molecules) and t_h (hole transfer ability, which depends on the overlap of the highest occupied molecular orbital (HOMO) between molecules). Higher values of t_e and t_h indicate more efficient electron and hole transfer between molecules, thereby facilitating the charge-transfer process.

The J_{CT} mechanism is highly sensitive to the stacking geometry of molecules (i.e., the arrangement of molecules in three-dimensional space), particularly the lateral alignment (intermolecular displacement), which significantly affects the spatial overlap between the HOMO and LUMO orbitals. Stacking configurations with stronger intermolecular overlap, such as slip stacking, help increase the values of t_e and t_h, thereby enhancing charge-transfer capability. As a result, J_{CT} significantly alters the electronic structure of the excited state by enhancing intermolecular charge transfer, making the excited state more stable. This leads to a notable reduction in the energy level of the first excited state (S_1), triggering a significant redshift in the absorption spectrum [62]. In contrast, J_{Coul} is a long-range, weak intermolecular interaction that has a minimal effect on the excited state energy levels, typically resulting in a smaller redshift or blue-shift.

2.2. H-Aggregate

According to the molecular aggregate exciton model, when the slip angle of the coplanar parallel stacking of molecules exceeds 54.7°, H-aggregates are formed (Figures 2B and 3A). In H-aggregates, the transition dipoles of the molecules are arranged in a "face-to-face" parallel stacking configuration, where the two split energy levels of the low exciton state, arising from dipole–dipole interactions, are typically optically forbidden, while the high exciton state is optically allowed (Figure 2B). This structure has two significant effects on the optical properties of H-aggregates: (1) The main absorption peak typically blue-shifts compared to the monomer, corresponding to the optically allowed

high exciton state. (2) Since the low exciton state, corresponding to the emission state, is optically forbidden, H-aggregates exhibit a lower radiative decay rate and suppressed fluorescence emission, which is the core characteristic of "aggregation-caused quenching" (ACQ) behavior.

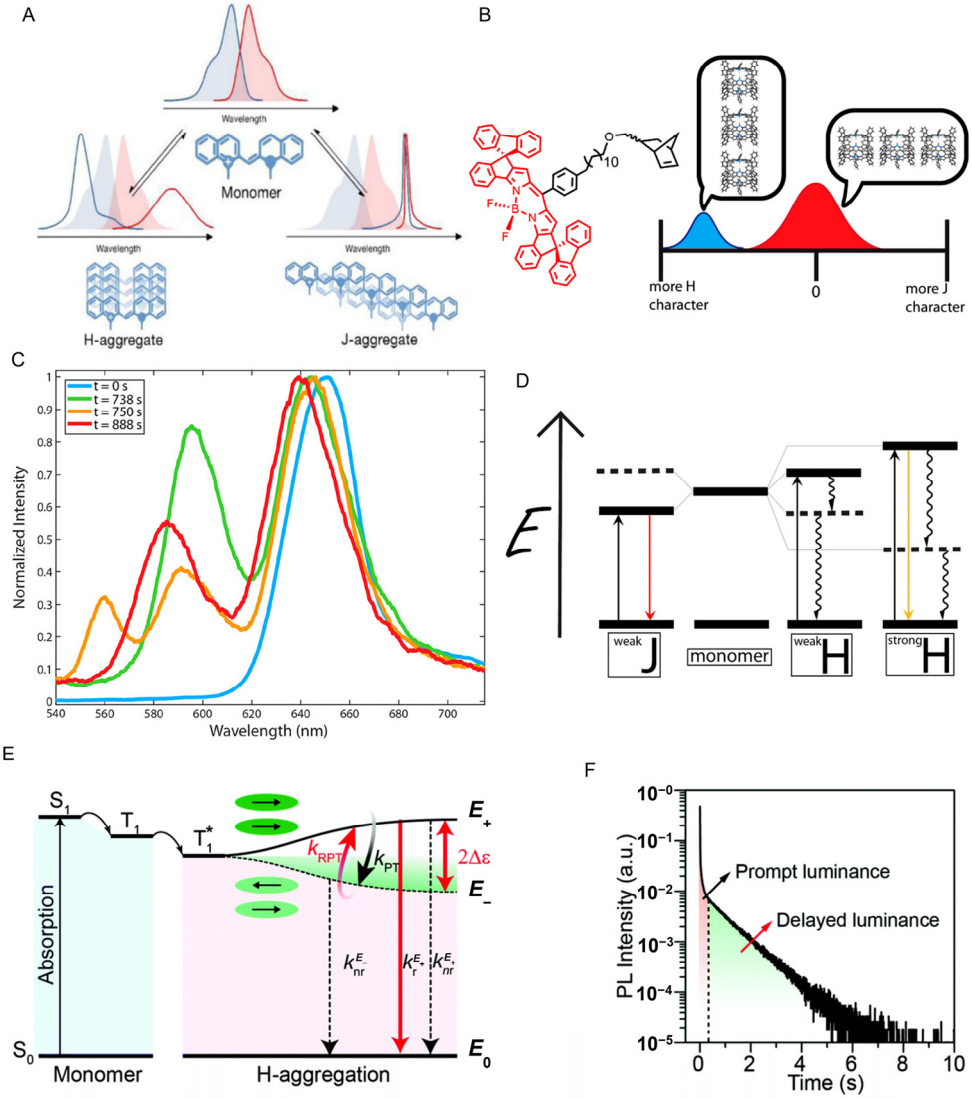

Figure 3. (**A**) Schematic illustrations of face-to-face H-aggregate and slip-stacked J-aggregate and the changes in absorption (blue) and fluorescence (red) spectra from a pseudoisocyanine (PIC) dye monomer. (**B**) Schematic diagram of the structure of a BODIPY-labeled fluorescent norbornene monomer and its H-aggregate fluorescence emission. (**C**) Spectra of a single monomer particle spin-coated from a toluene–isopropanol mixture over time and selected normalized spectra at several time points chosen to highlight emission from the blue satellite. (**D**) Jablonski diagram, showing emissive properties of observed aggregates. Weakly J-coupled aggregates are expected to demonstrate red emission, similar to the solution-phase monomer. Weakly H-coupled aggregates are expected to be non-emissive due to rapid internal conversion to the non-emissive lower exciton level. Strongly H-coupled aggregates will possess a large energetic splitting between the upper and lower exciton bands that will slow internal conversion, allowing weak emission from the upper exciton state. (**E**) Schematic representation of the organic, ultralong, room-temperature phosphorescence (OURTP) mechanism in H-aggregation. (**F**) OURTP (545 nm) decay curve of pCNPhCz at room temperature. The images are reproduced with permission from [32,63,64].

In H-aggregates, the excitons are in a higher excitation state with a larger energy gap, and when they transition back to the ground state, they undergo a rapid internal

conversion process that transfers them to an optically forbidden dipole state. During this process, non-radiative species gradually accumulate, and ultimately, the system relaxes to the ground state through further internal conversion [32] (Figure 3D). Although the optical transition to the low exciton state is forbidden in most H-aggregates, fluorescence can still be observed under certain special conditions. For example, some studies have observed a redshifted fluorescence emission from H-aggregates, indicating that the fluorescence originates from the low exciton state. This phenomenon could be due to factors such as changes in the intermolecular stacking angle, solvent effects, or external perturbations that break the symmetry of the system, allowing for partial radiative transitions from the low exciton state [65,66].

Some studies have also reported the rarely observed phenomenon of blue-shifted emission from H-aggregates [67]. For example, Goldsmith et al. [32] found fluorescence emission originating from the higher exciton state when studying H-aggregates formed by functionalized BODIPY molecules (Figure 3B,C). They noted that the emission from the higher exciton state is associated with strong coupling in H-aggregates. In these aggregates, the large energy gap between the high and low exciton states leads to a significant reduction in internal conversion, allowing the excitons to directly emit from the high exciton state (Figure 3D). This phenomenon violates the Kasha rule (which states that photons are typically emitted only from the lowest excited state). Another phenomenon of H-aggregate luminescence was reported by the research teams of Fan and Chen [64]. They discovered an H-aggregate afterglow luminescence and quantitatively analyzed the effect of H-aggregate formation on organic afterglow properties using exciton theory. They found that the organic afterglow was caused by a transition-allowed high-energy radiative transition: triplet excitons, captured by the H-aggregates, overcame the exciton splitting energy under thermal assistance and transitioned from the transition-forbidden low-energy state (dark state) to the transition-allowed high-energy state (bright state) of the H-aggregate, resulting in room-temperature organic afterglow emission (Figure 3E,F).

2.3. Aggregation-Induced Emission

Aggregation-induced emission (AIE) refers to the phenomenon where certain molecules exhibit weak or no luminescence in dilute solution but show significantly enhanced emission in aggregated or solid states [68]. In fact, AIE is not a completely new concept. As early as 1853, Stokes observed that some inorganic salts exhibited strong luminescence in the solid state but showed weaker emission in solution, a phenomenon similar to AIE [69]. However, due to the lack of in-depth theoretical explanation and exploration of potential applications at the time, AIE did not receive significant attention. It was not until 2001 that Tang et al. [68] systematically revealed the AIE phenomenon by studying methylpentaphenylsilane, a compound rich in molecular rotor groups, laying the foundation for AIE research. In their study, the molecule was almost non-emissive in solution but showed a significant increase in luminescence intensity when forming nanoscale aggregates (Figure 4A,B). Further research showed that AIE-active groups exhibit active intramolecular motions in the excited state, particularly intramolecular rotational movements, which can accelerate non-radiative decay, leading to fluorescence quenching in the solution state. Specifically, in solution, intramolecular rotation and vibration can promote non-radiative pathways, thus suppressing emission. However, when these molecules aggregate or are in the solid state, the intermolecular interactions restrict the intramolecular rotation and vibration, suppressing non-radiative decay and enhancing the emission.

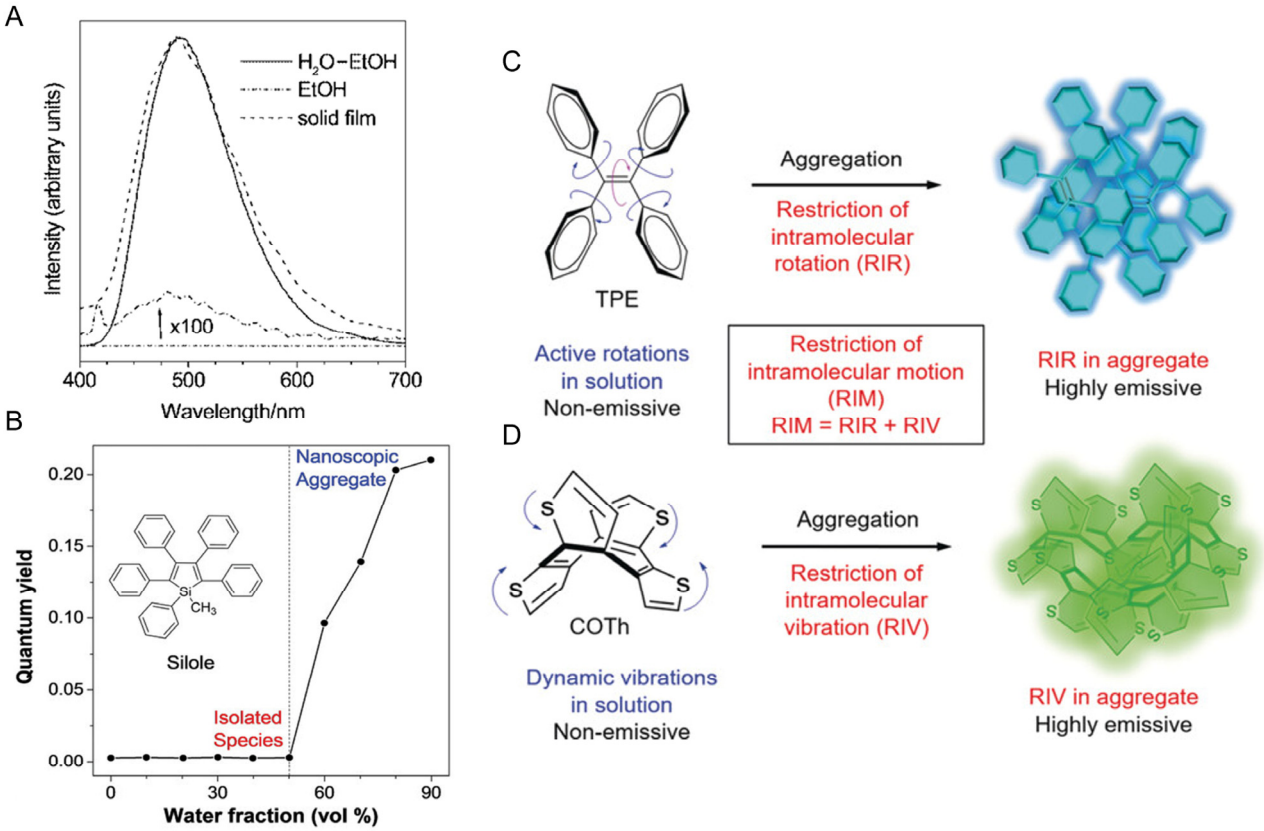

Figure 4. (**A**) PL spectra of methylpentaphenylsilane in water–ethanol mixture (90:10 by volume), absolute ethanol, and solid film; concentration of 1:10 μM; excitation wavelength (nm): 381 (for solutions) and 325 (for film). The 100-times magnified data gave a noisy spectrum. (**B**) Quantum yield of methylpentaphenylsilane vs. solvent composition of the water–ethanol mixture. (**C**) Tetraphenylethene (TPE) is non-emissive when dissolved but becomes emissive when aggregated due to the restriction of intramolecular rotations (RIRs). (**D**) Cyclooctatetrathiophene (COTh) shows AIE activity due to the restriction of intramolecular vibration (RIV) in the aggregated state. The images are reproduced with permission from [68,70].

Based on this, Tang et al. proposed the "Restriction of Intramolecular Rotation" (RIR) mechanism [70] as the fundamental principle to explain the AIE phenomenon. To further explain AIE systems that do not contain molecular rotors, Tang et al. introduced the "Restriction of Intramolecular Vibration" (RIV) mechanism, suggesting that intramolecular vibrations can also promote non-radiative decay. The RIV mechanism complements the RIR mechanism by indicating that even in the absence of molecular rotors, intramolecular vibrational motions may influence fluorescence quenching. Ultimately, the RIR and RIV mechanisms were integrated into a more comprehensive explanatory framework—the "Restriction of Intramolecular Motion" (RIM) mechanism (Figure 4C,D)—which has been widely accepted as the primary mechanism underlying AIE phenomena [71]. According to the RIM mechanism, any strategy that limits the intramolecular motion of luminescent molecules can theoretically enhance their emission properties [72]. The unique luminescent characteristics of AIE molecules have led to their broad application prospects in fields such as fluorescence imaging, biosensing, photosensitizing drugs, and optoelectronic devices [70].

3. Biological Applications of NIR-II Organic Molecular Aggregates

In the past decades, many organic molecules have been rationally designed and self-assembled into aggregates, which exhibit unique and excellent photophysical properties.

These aggregates show great potential for applications in bioimaging, disease diagnosis, and treatment. This section summarizes some of the types of organic molecular aggregates that have been reported and provides relevant examples to illustrate their characteristics and application areas (Figure 5 and Table 1).

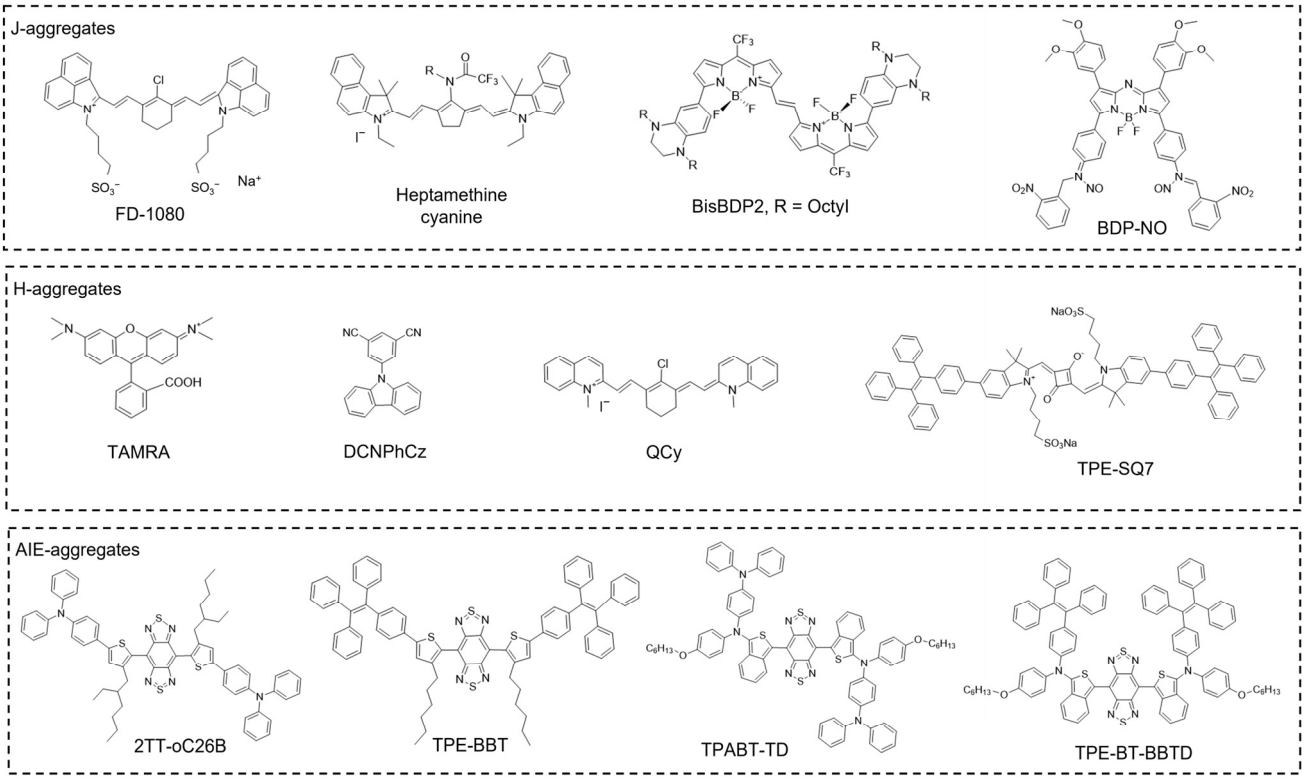

Figure 5. Structures of the representative organic molecule for self-assembled aggregates.

Table 1. The optical properties and application of aggregates in Figure 5 (n.a. = not available).

Aggregates	Molecules	Type	λabs/λem [nm]	QYs [%]	Applications	Refs
FD-1080 J-aggregates	FD-1080	J-type	1360/1370	n.a.	Vessel imaging and the detection of inflammation	Zhang et al., 2019 [47]
CYJ1007, CYJ1059 et al.	Heptamethine cyanine	J-type	1007/1009 1059/1060	0.36/0.21	Multiplexed PAI and FL imaging in animals	Zhao et al., 2024 [73]
BisBDP2 J-aggregate	BisBDP2	J-type	1300/n.a.	n.a.	PAI and deep-tumor PTT	Liu et al., 2022 [26]
BDP-NO@PEG-b-PCL	BDP-NO	J-type	820/n.a.	n.a.	Anti-infection therapy	Hu et al., 2022 [74]
Av-TAMRA	TAMRA	H-type	520/n.a.	n.a.	Activatable in vivo molecular imaging	Kobayashi et al., 2009 [75]
DCNPhCz NPs	DCNPhCz	H-type	544/593	8.6	Live-cell imaging	Fan and Chen et al., 2019 [64]
QCy NPs	QCy	H-type	648/n.a.	n.a.	PAI-guided tumor PTT	Yin et al., 2022 [76]
TPE-SQ7 NPs	TPE-SQ7	H-type	635/n.a.	n.a.	PDT and PTT	Li et al., 2024 [27]

Table 1. *Cont.*

Aggregates	Molecules	Type	λabs/λem [nm]	QYs [%]	Applications	Refs
2TT-oC26B NPs	2TT-oC26B	AIE-type	730/1031	11.5	NIR-IIb FL imaging of blood vasculature	Tang et al., 2020 [77]
TPE-BBT PLNPs	TPE-BBT	AIE-type	660/955	31.5	FL and chemiluminescence (CL)-based bioimaging	Tang and Zhang et al., 2022 [78]
TPABT-TD NPs	TPABT-TD	AIE-type	1025/1328	n.a.	FL, PAI, and photothermal imaging-guided PTT	Wang et al., 2024 [79]
BBTD@PM NPs	TPE-BT-BBTD	AIE-type	993/1305	n.a.	FL imaging-guided PTT of tuberculosis	Liao et al., 2024 [80]

3.1. Applications of Organic Molecular Aggregates in In Vivo Imaging

In recent years, J-aggregates have shown tremendous potential in imaging applications such as angiography, drug delivery, and biomarker indication [17,46,59,81–90]. For instance, in 2019, Zhang et al. [47] successfully developed FD-1080 J-aggregates, which were formed by self-assembled FD-1080 and 1,2-dimyristoyl-sn-glycero-3-phosphocholine (DMPC) (Figure 6A). Transmission electron microscope (TEM) images and dynamic light scattering (DLS) showed uniform and monodispersed J-aggregates with a size of 110 ± 10 nm. This J-aggregate exhibited absorption and emission characteristics beyond 1300 nm, which were bathochromically shifted about 300 nm compared to the FD-1080 monomer (Figure 6B). In vivo bioimaging of hindlimb and cerebral vasculature demonstrated that J-aggregates achieved a higher spatial resolution and signal to background (SBR) beyond the 1500 nm window (Figure 6C), which were successfully employed to monitor dynamic changes in the carotid arteries of hypertensive rats following the administration of the antihypertensive drug Isoket (isosorbide dinitrate) (Figure 6D,E).

In 2024, Zhao et al. [73] successfully synthesized more than ten types of J-aggregates with extremely sharp spectral bandwidths (full width at half maximum ≤ 38 nm) by introducing trifluoroacetyl and benzyl substituents at the meso-position of a heptamethine benzindolecyanine molecule backbone. By fine-tuning the benzyl group, they achieved precise modulation of the optical properties of the J-aggregates (Figure 6F). The crystallographic data revealed the molecular packing of the J-aggregates, offering valuable insights into the molecular organization and its influence on the optical characteristics. Furthermore, some of these J-aggregates have been successfully applied in NIR-II fluorescence and PA multispectral imaging of multiple organs in vivo, demonstrating their potential for advanced biomedical imaging (Figure 6G,H).

H-aggregates typically result in broadened absorption bands, reduced absorbance, and fluorescence quenching [91]; thus, its disassembly corresponding to dye monomer fluorescence recovery was used for luminescence imaging. For example, in 2009, Kobayashi et al. [75] conjugated rhodamine derivatives (R6G and TAMRA) with Avidin, a protein targeting the d-galactose receptor, and Trastuzumab, an antibody targeting the HER2/neu antigen (Figure 7A). In fluorescence endoscopic molecular imaging experiments, researchers injected the highly quenched probe (Avidin–TAMRA) and the minimally quenched probe (Avidin–Alexa488) into mice with peritoneal ovarian metastases, respectively. The experimental results demonstrated that the utilization of Avidin–TAMRA facilitated the clear visualization of the tumor site with minimal background fluorescence, whereas the employment of Avidin–Alexa488 resulted in elevated background fluorescence, thereby hindering the imaging of the tumor (Figure 7B). Consequently, the fluorescence burst mechanism of H-aggregates can be employed to develop activatable in vivo molecular imaging probes,

thus enhancing the specificity and sensitivity of imaging procedures. In 2019, Fan and Chen et al. [64] successfully developed a series of CN-substituted phenylcarbazole isomer organic afterglow materials through molecular design and H-aggregate engineering. The organic afterglow was attributed to a transition-allowed high-energy radiative transition: triplet excitons, captured by H-aggregates, transitioned from a low-energy forbidden state (Dark state) to a high-energy allowed state (Bright state) under thermal assistance, resulting in organic, ultralong, room-temperature phosphorescence (OURTP) with a lifetime of up to 0.92 s and a quantum efficiency of 8.6% (Figure 7C). The team also developed phosphors (DCNPhCz NPs) for live-cell imaging (Figure 7D,E), which emitted light for several seconds after excitation was removed. This characteristic made them particularly attractive for cellular imaging, offering extremely low background noise in bioluminescent systems (Figure 7F).

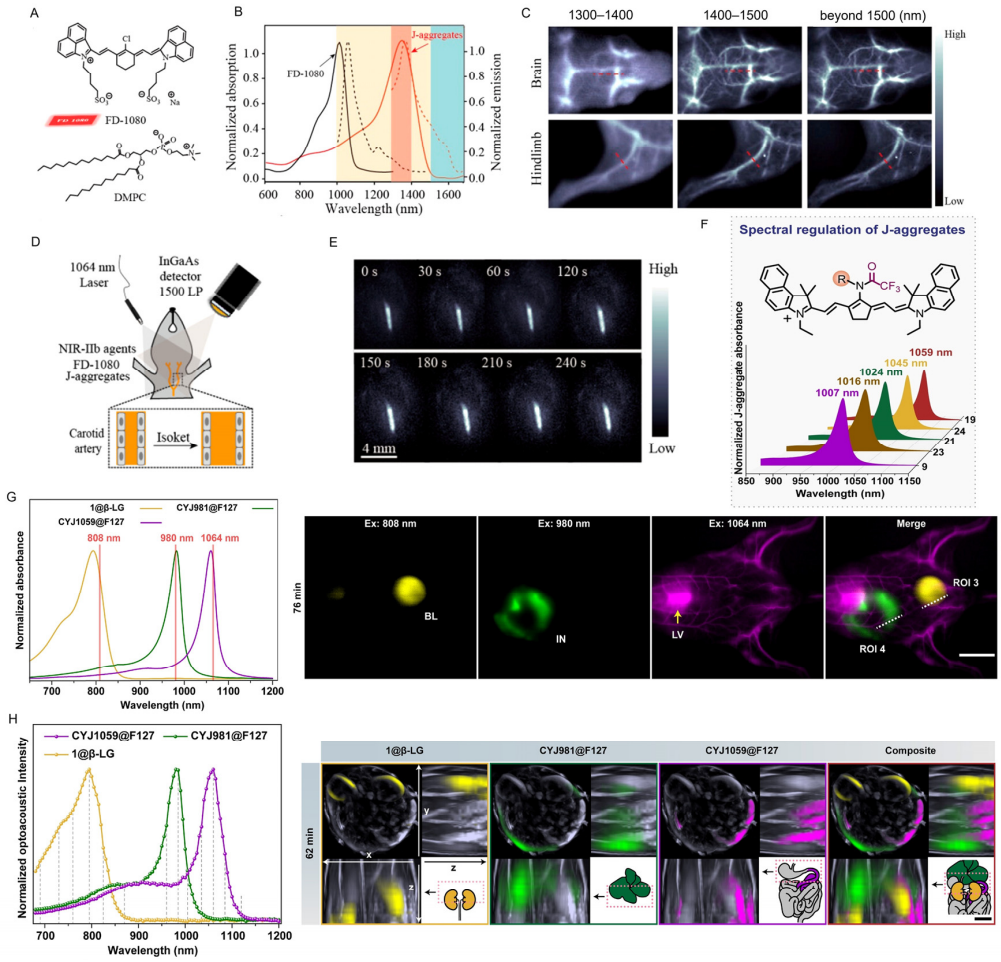

Figure 6. (**A**) Structure of FD-1080 and DMPC. (**B**) Normalized absorption (solid lines) and emission (dashed line) of FD-1080 monomer and J-aggregates. (**C**) Images of brain and hindlimb vessels achieved by J-aggregates in varied regions. (**D**) Schematic illustration of the hypotensive process. (**E**) Dynamic bioimaging of carotid artery after administration of Isoket beyond 1500 nm window achieved by J-aggregates. (**F**) Fine-tuning the benzyl group enables spectral regulation of J-aggregates. (**G**) Normalized absorption spectra of 1@β-LG, CYJ981@F127, and CYJ1059@F127, along with representative NIR-II fluorescence images excited at 808, 980, and 1064 nm, and the merged image at 76 min (in the supine position). BL: bladder; IN: intestine; LV: liver. Scale bar: 1 cm. (**H**) Normalized optoacoustic intensities for the three dyes, with dashed vertical lines indicating the 13 irradiation wavelengths for three-color in vivo imaging, and representative 3D MSOT images reflecting the biodistribution of the three dyes in a mouse at 62 min. Scale bar: 0.5 cm. The images are reproduced with permission from [47,73].

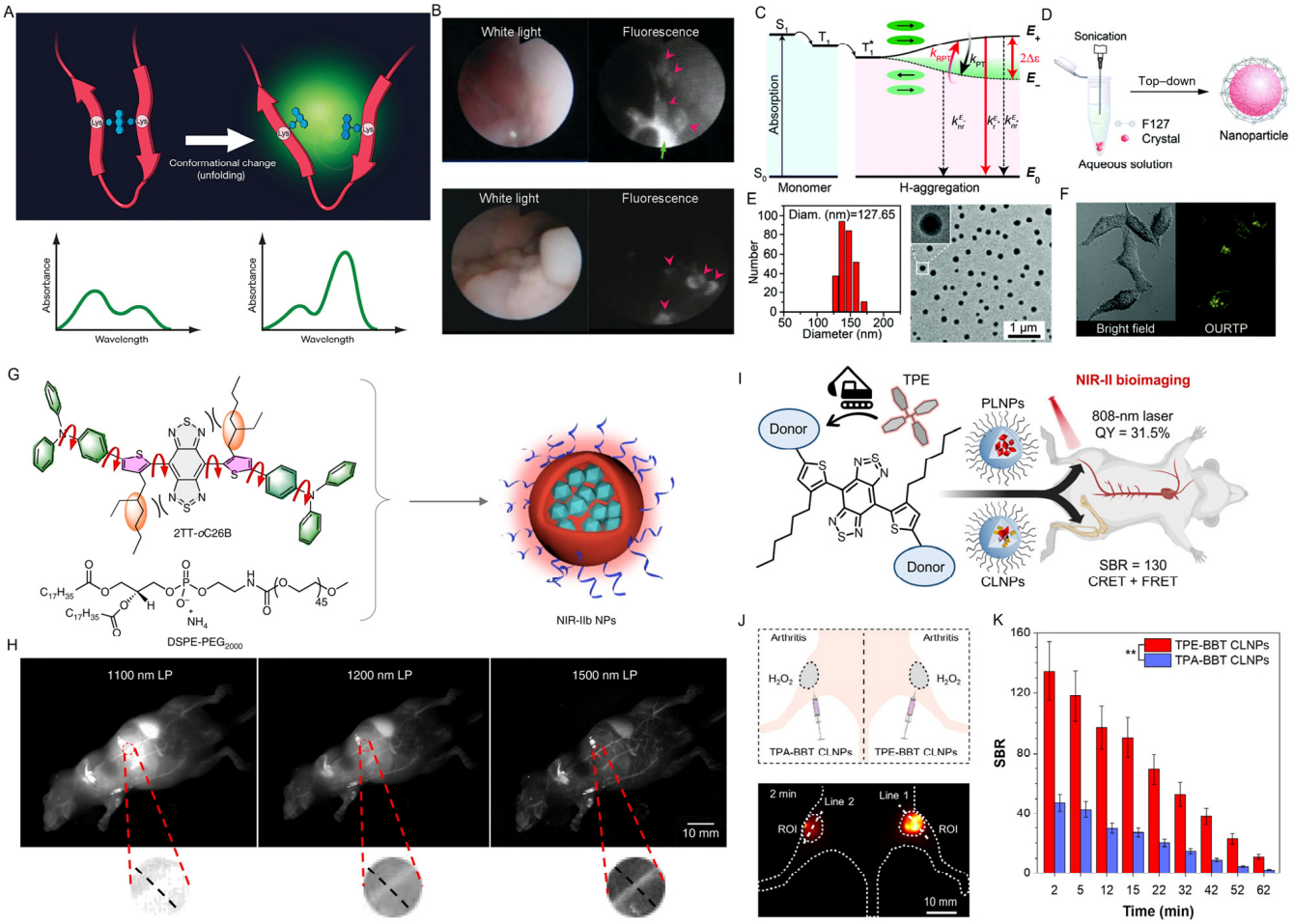

Figure 7. (**A**) Schema of quenching and activation mechanism employing H-dimer formation after binding to the protein. (**B**) In vivo fluorescence endoscopic images in tumor-bearing mice enhanced by Av-Alexa488 (above) and Av-TAMRA (below). The pink arrow heads show the tumor nodules. The tumors were clearly visualized with the activatable probe Av-TAMRA. In contrast, Av-Alexa488, an always-on probe, showed high background signal and high fluorescence from excess injectate in the peritoneal cavity (green arrow). (**C**) Schematic representation of the OURTP mechanism in H-aggregation. (**D**) Top–down route to prepare DCNPhCz NPs. (**E**) Diameter distribution, and TEM images of DCNPhCz NPs. (**F**) Confocal laser scanning microscopy images of living HeLa cells incubated with the NPs. The yellow channels were acquired by collecting the luminescence from 525 to 625 nm under the excitation of a 405 nm laser. (**G**) Schematic illustration of 2TT-oC26B NPs. (**H**) Comparison of NIR-II fluorescence signals for whole-body imaging of living mice in an area close to the liver under different LP filters treated with 2TT-oC26B NPs. (**I**) Schematic illustration of rational design of NIR-II AIEgens with ultrahigh quantum yields for photo- and chemiluminescence imaging. (**J**) Schematic illustration of chemiluminescence (CL) imaging of the arthrosis in mice. (**K**) Signal-to-background ratios (SBRs) of the CL intensity in the ROI as a function of post-injection time after the injection of TPE-BBT and TPA-BBT CLNPs. ** $p < 0.01$; data represent means ± SD; n = 3. The images are reproduced with permission from [27,64,75–78].

Extending the conjugation length of organic dyes is a common strategy to achieve redshifted emission. However, when these large π-conjugated systems are in aggregated states or nanoparticle forms, as commonly encountered in biological applications, strong intermolecular π–π interactions often lead to fluorescence quenching [92]. In contrast, AIE aggregates exhibit strong fluorescence in the aggregated state, demonstrating significant potential for applications. In 2020, Tang et al. [77] successfully prepared nanoparticles (NIR-IIb NPs) based on the 2TT-oC26B molecule using the twisted intramolecular charge-transfer (TICT) and AIE strategies, which were applied for high-quality in vivo NIR-IIb

fluorescence imaging (Figure 7G). The emission spectrum of the NIR-IIb NPs extended to 1600 nm with an exceptionally high fluorescence quantum yield (QY), reaching 11.5% across the entire NIR-II region (1000–1600 nm), and even in the NIR-IIb region (1500–1600 nm), the QY remained 0.12%. Furthermore, NIR-IIb NPs not only provide a research platform for NIR-IIb fluorescence imaging of the blood vasculature and intestinal tract but also offer new insights into the development of organic molecules with an ultralong emission wavelength and high brightness (Figure 7H).

In 2022, Tang and Zhang et al. [78] collaborated to design and synthesize the AIE-active NIR-II emissive dye TPE-BBT and its methoxy derivative TPEO-BBT, using tetraphenylethylene (TPE) as the electron donor to replace triphenylamine (TPA) in the molecular design. They investigated the applications in fluorescence and chemiluminescence (CL)-based bioimaging. Using IR-26 as a reference with a fluorescence quantum yield (QY) of 0.5%, TPE-BBT and TPEO-BBT exhibited ultrahigh relative QYs of 31.5% and 23.9% in water, respectively. Further investigation revealed that the crystals of TPE-BBT exhibited an absolute QY of 10.4%, which is also the highest absolute QY reported for NIR-II organic small-molecule dyes (Figure 7I). In arthrosis inflammation imaging using NIR-II CL nanoparticles (NPs), TPE-BBT generated strong NIR-II CL signals, with a peak SBR of about 130 in the inflammation area, remaining above 10 even after 62 min. TPE-BBT CLNPs outperformed TPA-BBT in CL imaging, highlighting the importance of NIR-II energy acceptor QYs. These results demonstrate TPE-BBT's great potential for CL imaging and sensing (Figure 7J,K).

3.2. Application of Organic Dye Aggregates in Disease Diagnosis and Treatment

J-aggregates show great potential in the diagnosis and treatment of tumors, inflammation, and other complex diseases [93–98]. In 2022, Liu et al. [26] successfully prepared the BisBDP2 J-aggregate based on BisBDP2 molecules (Figure 8A). The BisBDP2 J-aggregate exhibited an absorption peak around 1300 nm (Figure 8B), along with exceptional photothermal conversion performance, featuring strong PA signals and a high photothermal conversion efficiency of 63% (Figure 8C). In vivo experiments demonstrated that BisBDP2 J-aggregates exhibited significant potential in PA imaging and deep-tumor photothermal ablation (Figure 8D–F). PA imaging enabled precise tumor localization, facilitating efficient PTT and significantly suppressing tumor growth (Figure 8G–I). This study establishes a solid foundation for the development of NIR-II-absorbing J-aggregates and provides strong support for their broad application in future biophotonics technologies.

In 2022, Hu et al. [99] developed a novel NIR J-aggregate based on BDP-NO molecules (Figure 8J,K), which exhibited both an exceptional photothermal conversion efficiency and the ability to release nitric oxide (NO). Through molecular dynamics simulations, it was shown that the BDP-NO molecules could self-assemble with PEG-b-PCL diblock copolymers in aqueous solutions, forming stable J-aggregates. In this system, the hydrophobic BDP-NO molecules were encapsulated within the micellar core of the PEG-b-PCL nanoparticles, which provided a favorable environment for their assembly (Figure 8N,O). The J-aggregate not only exhibited a high photothermal conversion efficiency under NIR light but also had the unique ability to release NO upon irradiation (Figure 8L,M). The photothermal effect enabled the BDP-NO J-aggregate to efficiently eliminate pathogens and disrupt bacterial biofilms by releasing NO, thereby further enhanced the therapeutic effect. The experimental results showed that this combined treatment strategy has good inhibitory effects on various drug-resistant strains, providing a new approach for anti-infection therapy (Figure 8P).

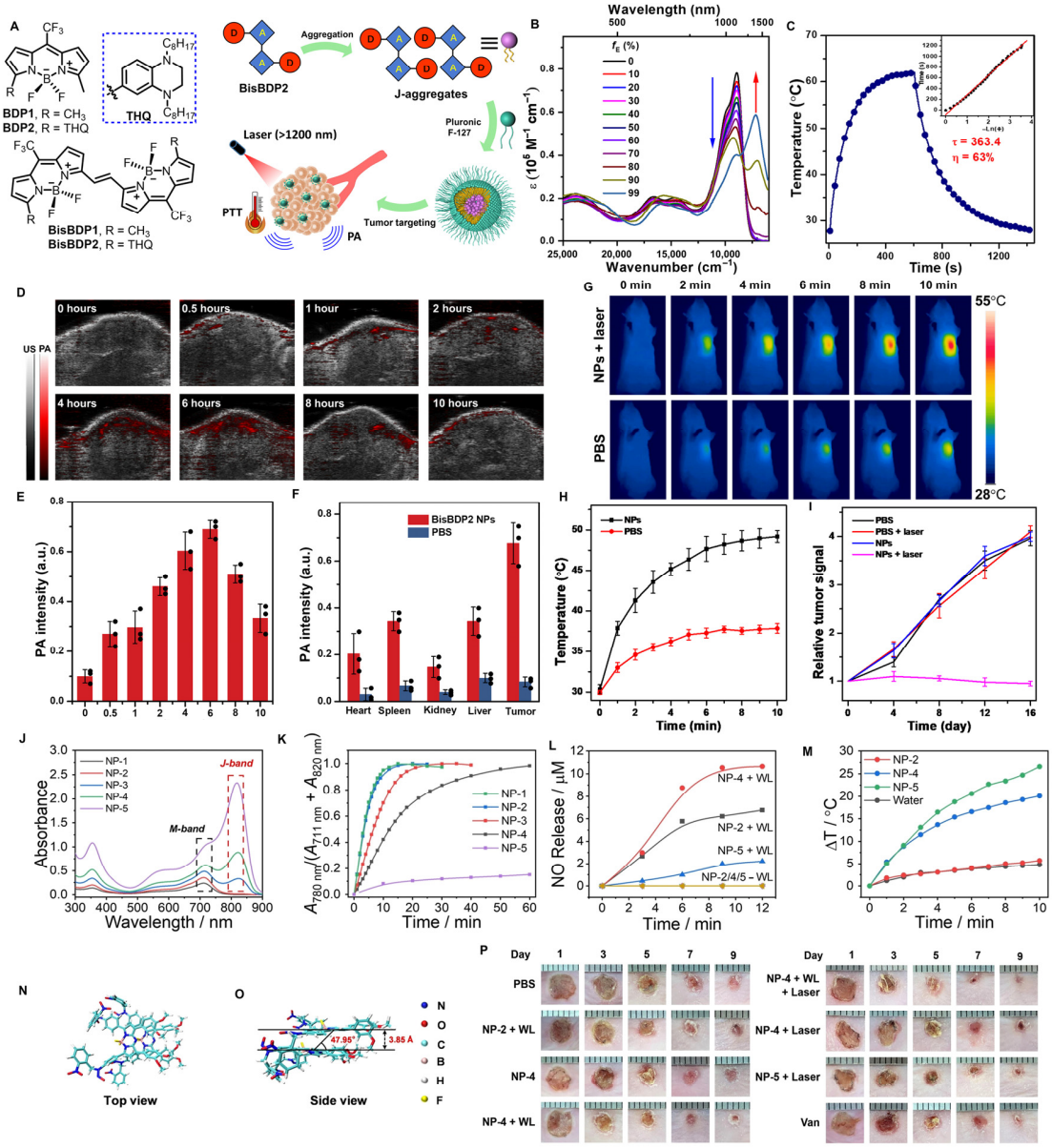

Figure 8. (**A**) Chemical structures of BDP1, BDP2, BisBDP1, and BisBDP2 and schematic illustration of the PA imaging-guided PTT in the NIR-II window using BisBDP2 J-aggregates. (**B**) J-aggregation behavior of BisBDP2 in tetrahydrofuran–ethanol binary solvents with varied volumetric fractions of ethanol (f_E). (**C**) Photothermic heating curves of BisBDP2 NP dispersions under 1208 nm irradiation for 10 min followed by cooling to room temperature. Inset: Linear correlation of the cooling times versus negative natural logarithm of driving force temperatures. (**D**) PA images of the orthotopic liver tumor at different times after injection of BisBDP2 NPs at the tail vein. (**E**) PA intensity from (**D**) plotted as a function of time after injection. (**F**) PA images of major organs under 1260 nm irradiation at 6 h post-injection of PBS and BisBDP2 NPs at the tail vein. (**G**) Infrared thermal imaging of orthotopic liver tumor mice treated with PBS and BisBDP2 NPs exposed to 1208 nm laser recorded at different time intervals, respectively. (**H**) Temperature profiles of tumor site as a function of irradiation time. (**I**) Relative orthotopic liver tumor fluorescence intensity of the mice during different treatments. (**J**) UV–vis spectra of micellar nanoparticles of NP-1–NP-5. (**K**) Evolution of UV–vis spectra of NP-1–NP-5 under WL irradiation. (**L**) Cumulative NO release determined using Griess assay of NP-2, NP-4, and NP-5 micelles under WL irradiation. (**M**) Temperature changes of aqueous dispersions of NP-2, NP-4, and NP-5 micelles under 808 nm laser irradiation. (**N**) Top and (**O**) side views of BDP-NO J-aggregates within PEG-b-PCL micelles. (**P**) Photographs of cutaneous wounds of MRSA-infected mice receiving various treatments. The images are reproduced with permission from [26,74].

H-aggregates, due to the unique molecular stacking structure, significantly enhance the non-radiative transition efficiency of molecules and show great potential in disease treatment, particularly in PTT. H-aggregates can efficiently convert light energy into heat, enabling precise tumor ablation. In 2022, Yin et al. [76] developed stable H-aggregate nanoparticles (QCy NPs) based on a quinoline cyanine (QCy) with symmetric rigid planar structures (Figure 9A). In aqueous solution, the planar QCy were able to form close π–π molecular stacking, facilitating self-assembly into stable H-aggregates at low concentrations. QCy NPs significantly enhanced the photostability and photothermal conversion efficiency of the monomeric molecules, with the photothermal conversion efficiency increasing from 20.1% (non-H-aggregated) to 63.8% (QCy NPs) (Figure 9A,B), which achieved efficient PA imaging-guided tumor PTT at a low dosage (Figure 9C–F).

In 2024, Li et al. [27] developed a stable H-aggregate (TPE-SQ7 NPs) based on the supramolecular photosensitizer TPE-SQ7 in nonpolar solvents and aqueous solutions. The TPE-SQ7 NPs effectively suppressed the radiative transition process, promoting non-radiative transitions and intersystem crossing (ISC) (Figure 9G). Under 635 nm laser irradiation, they achieved high photothermal conversion efficiency (54.2%) and generated significant amounts of type I ROS (•OH) (Figure 9H). In vitro and in vivo experiments demonstrated that even in hypoxic conditions, the TPE-SQ7 NPs exhibited excellent anti-tumor efficacy, making them ideal candidates for combined PDT and PTT (Figure 9I–L). This study provided in-depth insights into the mechanism by which H-aggregates enhance type I PDT and offered valuable guidance for the development of supramolecular photosensitizers for combined PDT and PTT treatments.

AIE aggregates exhibit exceptional properties, such as strong fluorescence and enhanced photothermal and photodynamic effects in the aggregated state, making them highly promising for various therapeutic applications, particularly in PDT and PTT [99,100]. In 2024, Wang et al. [79] introduced an innovative AIE molecule, TPABT-TD (Figure 10A), which possesses NIR-II absorption capabilities and demonstrates remarkable fluorescence, photoacoustic, and photothermal effects. This molecule was designed for tri-modal imaging-guided NIR-II PTT of tumors. Through intramolecular donor–acceptor (D-A) interactions and AIE characteristics, the absorption peak and emission peak of TPABT-TD were located at 1025 nm and 1328 nm, respectively (Figure 10B,C). When TPABT-TD was encapsulated into water-dispersible nanoparticles (TPABT-TD NPs) (Figure 10E), the resulting nanoparticles exhibited significantly enhanced properties. Under 1064 nm laser irradiation, these nanoparticles showed a high photothermal conversion efficiency of up to 68.98% (Figure 10D), which was a critical factor in achieving effective tumor ablation through photothermal therapy. The strong photothermal effect enabled the precise targeting and destruction of tumor cells while minimizing the damage to surrounding healthy tissues (Figure 10E–G).

In 2024, Liao et al. [80] synthesized a molecule with AIE properties, TPE-BT-BBTD. Its fluorescence emission range extended to the NIR-IIb region and also exhibited efficient photothermal conversion capability. The researchers encapsulated TPE-BT-BBTD in a poly (lactic-co-glycolic acid) (PLGA) core using a nanoprecipitation method and then coated the nanoparticles' surface with the macrophage membranes stimulated by Mycobacterium marinum through a coextrusion process, resulting in the formation of BBTD@PM nanoparticles (PM stands for pre-activated macrophage membrane) (Figure 11A). After intravenous injection of BBTD@PM NPs into H37Ra-induced pulmonary tuberculosis (TB) mice, the NPs rapidly accumulated in the pulmonary granulomas and successfully achieved precise in situ imaging of individual granulomas. Furthermore, the NPs were able to selectively penetrate into the necrotic regions of granulomas, specifically targeting M. tuberculosis through receptor–ligand binding. By irradiating the thoracic cavity with 1064 nm laser, the

photothermal effect of BBTD@PM was activated, not only achieving targeted eradication of M. tuberculosis but also effectively alleviating pathological damage and decreasing the inflammation levels of lung tissues (Figure 11B). This strategy demonstrates significant advantages over conventional first-line antibiotic combination therapies and offers new insights for the clinical management of drug-resistant and drug-sensitive tuberculosis, showing great potential for application.

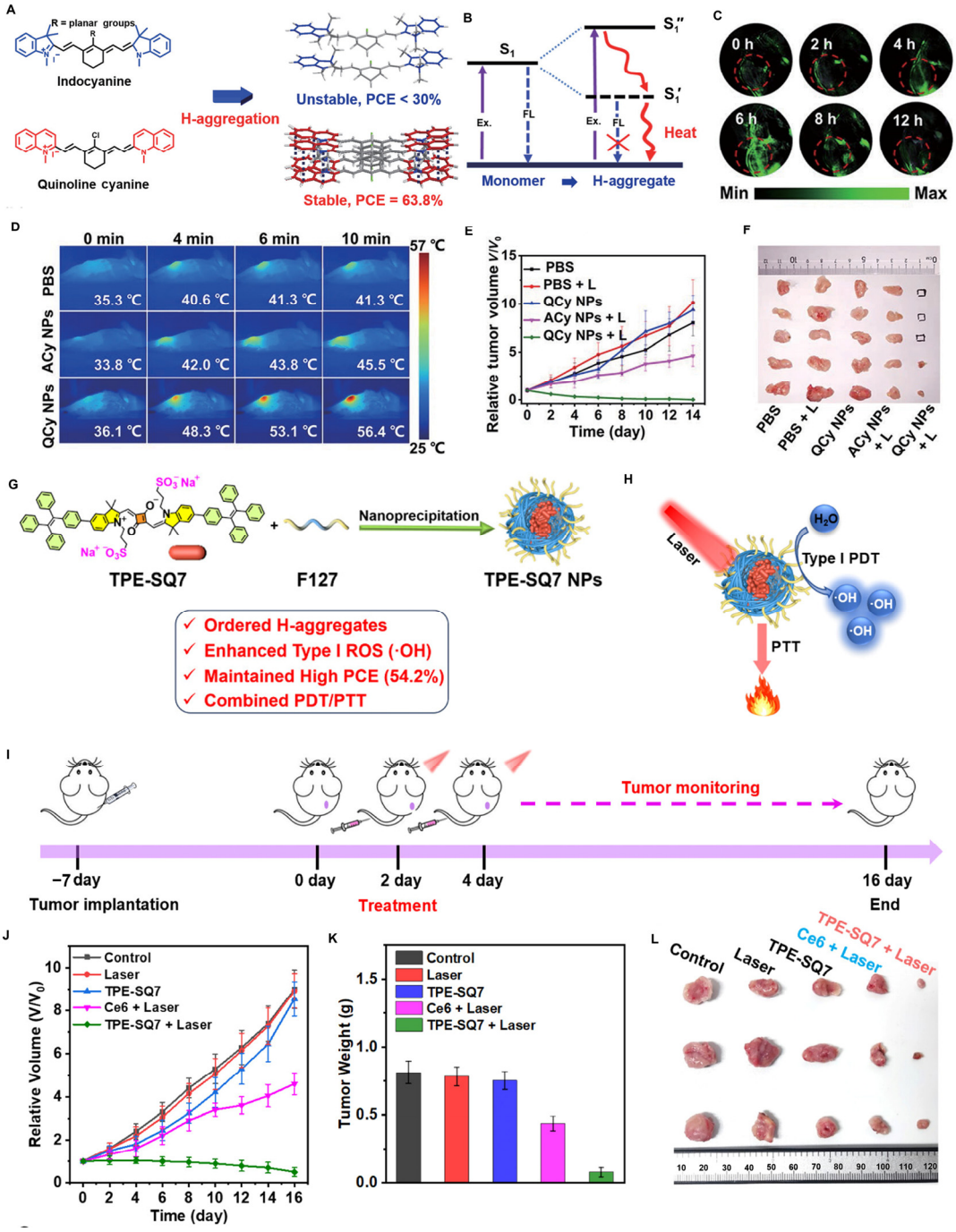

Figure 9. (**A**) Indocyanine and quinoline cyanine self-assemble into H-aggregates, showing different photothermal conversion efficiencies (PCEs). (**B**) H-aggregates significantly enhance the photothermal effect (Ex, excitation; FL, fluorescence; S_1, S_1', and S_1'', various electronic energy levels). (**C**) PA imaging in vivo at various times after intravenous injection of QCy NPs. (**D**) Photothermal images of 4Tl tumor-bearing mice injected intravenously with QCy NPs, ACy NPs, and PBS under 660 or

808 nm irradiation. (**E**) Change in tumor volume with time for each group of mice during treatments. (**F**) Images of tumors at the end of treatment. (**G**) Supramolecular H-aggregates of squaraines with enhanced type I photosensitization for combined PTT and PDT. (**H**) Schematic illustration of PTT/PDT of TPE-SQ6 and TPE-SQ7 NPs. (**I**) Schematic illustration of combined PDT and PTT treatment for a subcutaneous 4T1 tumor model in mice. (**J**) Time-dependent relative tumor growth curves of 4T1 tumor-bearing mice with different treatments. (**K**) Average tumor weights of 4T1 tumor-bearing mice under different treatments. (**L**) Photographs of tumor tissues from different treatments. The images are reproduced with permission from [27,76].

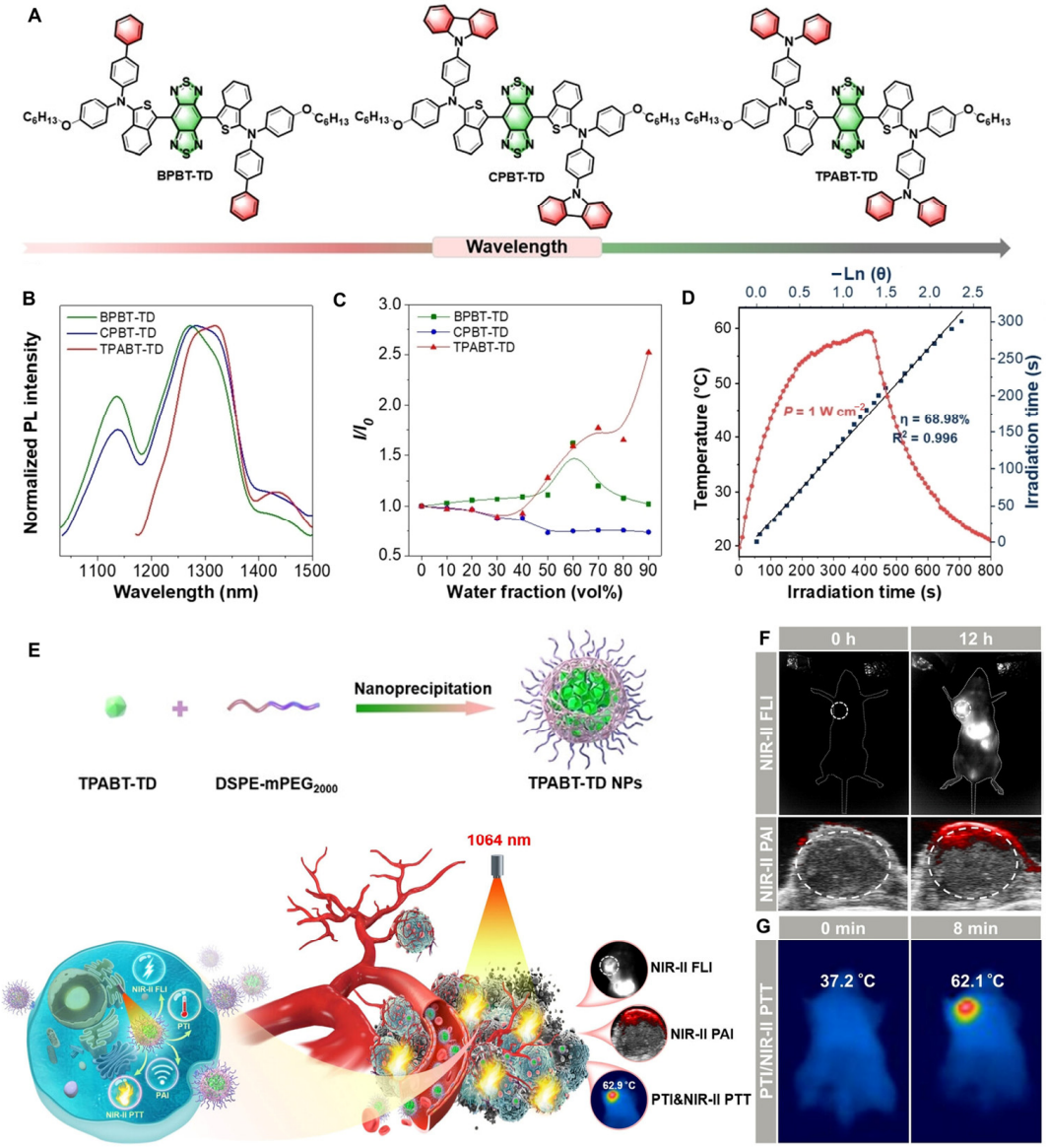

Figure 10. (**A**) The designed phototherapeutic molecules via subtle donor engineering. (**B**) Normalized photoluminescence spectra of the molecules dissolved in THF solution. (**C**) The plots of relative PL intensity (I/I_0) of the obtained compounds versus different water fractions. I_0 and I are the values of PL intensity at maximum peak in THF and THF/water mixtures, respectively. (**D**) PCE calculation of TPABT-TD NPs (100 μM). (**E**) Diagrammatic drawing of the encapsulation of NIR-II absorbing AIE nanoparticles and their application in photothermal eradication of orthotopic 4T1 breast tumor. (**F**) NIR-II FLI and NIR-II PAI of tumors at 0 and 12 h after treatment with TPABT-TD NPs. (**G**) PTI of 4T1 tumor-bearing mice at 0 and 8 min post-injection of TPABT-TD NPs under continuous 1064 nm laser irradiation at 12 h post-injection. The images are reproduced with permission from [79].

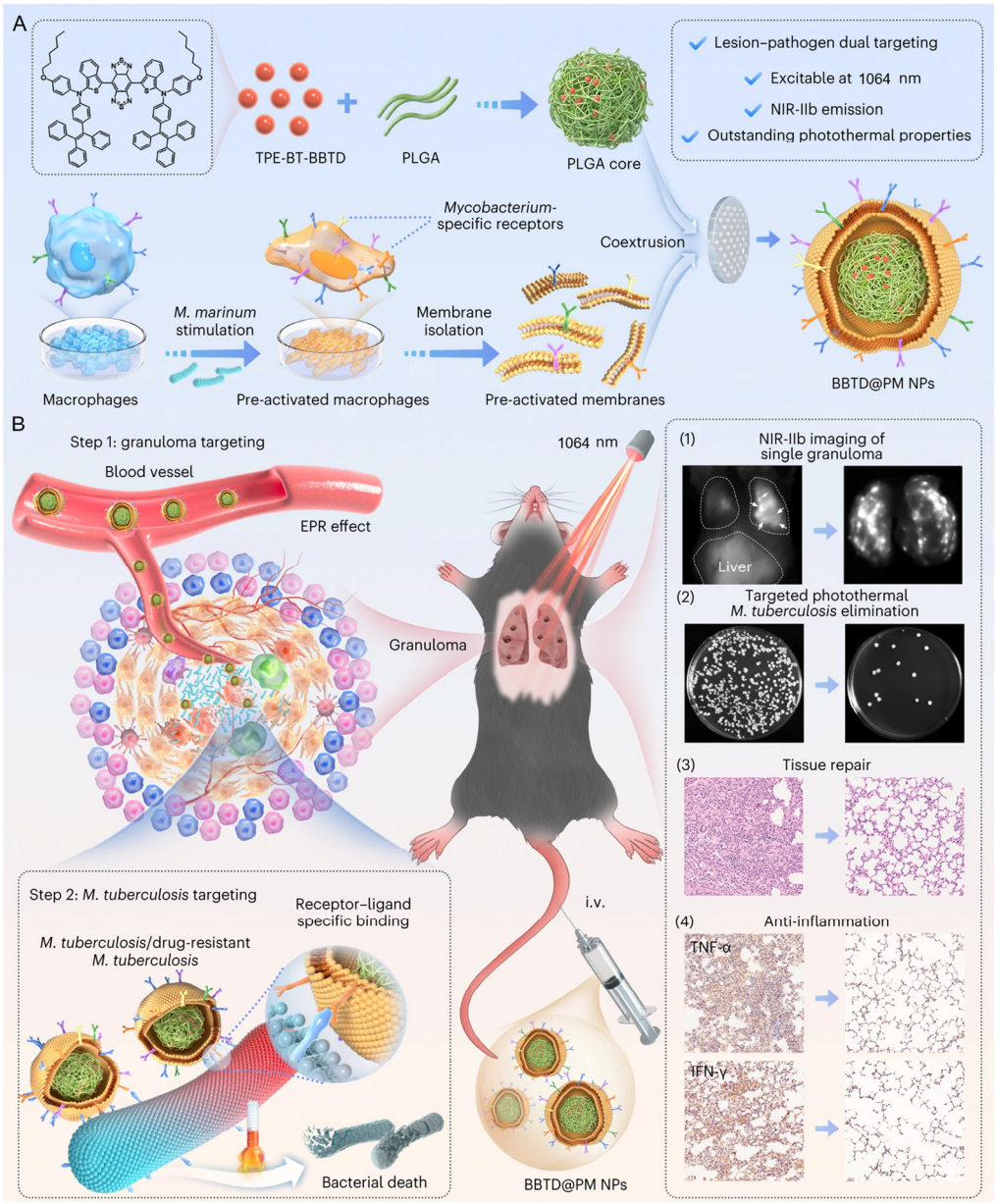

Figure 11. Schematic diagram of (**A**) BBTD@PM NP preparation and (**B**) BBTD@PM NP-mediated lesion–pathogen dual targeting and NIR-IIb imaging-guided PTT for TB. EPR, enhanced permeability and retention; i.v., intravenous injection; TNF-α, tumor-necrosis factor-α; IFN-γ, interferon-γ. The images are reproduced with permission from [80].

4. Conclusions and Perspectives

Overall, compared to monomers, organic molecular aggregates exhibit unique advantages in NIR-II imaging and disease treatment. These aggregates not only overcome interference in complex biological environments more effectively but also offer tunable spectral properties with more stable, stronger optical performance. They hold great promise for clinical applications due to their convenient functionalization, great flexibility, and good biocompatibility.

However, organic NIR-II aggregates still face challenges, especially in terms of optical stability and fluorescence quantum yield. Compared to inorganic probes, such as quantum dots or complexes of lanthanides and other metals, organic aggregates tend to have poorer optical stability, with prolonged exposure potentially leading to photobleaching or signal attenuation, affecting their performance in long-term imaging. Furthermore, the fluores-

cence quantum yield of organic NIR-II aggregates is generally lower than that of inorganic probes, which results in lower sensitivity and resolution for deep-tissue imaging. Moreover, considering the complexity of aggregate vectorization, controlling their aggregation states and maintaining their stabilities within the body remain a challenge. The environment and biological surrounding may affect the aggregation and dissociation process and impair their performance.

In the future, addressing these challenges may be achieved by optimizing their molecular structures to improve the optical stability and fluorescence quantum yield of NIR-II aggregates. Enhancing intermolecular interactions and improving aggregate stability would help boost their application in biomedical fields. Additionally, by introducing multifunctional strategies and combining organic NIR-II aggregates with other imaging and therapeutic technologies, multimodal imaging techniques could be developed to further enhance their performance in deep-tissue imaging, targeted therapy, and precise diagnosis.

Author Contributions: Conceptualization, K.W., R.Y. and Y.L.; investigation, K.W., R.Y. and X.S.; resources, Y.L.; writing—original draft preparation, K.W., R.Y. and X.S.; writing—review and editing, H.J. and Y.L. All authors have read and agreed to the published version of the manuscript.

Funding: This research was funded by the National Natural Science Foundation of China, grant number 22374073.

Conflicts of Interest: The authors declare no conflicts of interest.

References

1. Wang, T.; Wang, S.; Liu, Z.; He, Z.; Yu, P.; Zhao, M.; Zhang, H.; Lu, L.; Wang, Z.; Wang, Z.; et al. A hybrid erbium (III)-bacteriochlorin near-infrared probe for multiplexed biomedical imaging. *Nat. Mater.* **2021**, *20*, 1571–1578. [CrossRef]
2. Hong, G.; Antaris, A.L.; Dai, H. Near-infrared fluorophores for biomedical imaging. *Nat. Biomed. Eng.* **2017**, *1*, 0010. [CrossRef]
3. Chen, G.; Cao, Y.; Tang, Y.; Yang, X.; Liu, Y.; Huang, D.; Zhang, Y.; Li, C.; Wang, Q. Advanced near-infrared light for monitoring and modulating the spatiotemporal dynamics of cell functions in living systems. *Adv. Sci.* **2020**, *7*, 1903783. [CrossRef] [PubMed]
4. Chen, Y.; Wang, S.; Zhang, F. Near-infrared luminescence high-contrast in vivo biomedical imaging. *Nat. Rev. Bioeng.* **2023**, *1*, 60–78. [CrossRef]
5. Ji, Y.; Jones, C.; Baek, Y.; Park, G.K.; Kashiwagi, S.; Choi, H.S. Near-infrared fluorescence imaging in immunotherapy. *Adv. Drug Deliv. Rev.* **2020**, *167*, 121–134. [CrossRef]
6. Owens, E.A.; Henary, M.; El Fakhri, G.; Choi, H.S. Tissue-specific near-infrared fluorescence imaging. *Acc. Chem. Res.* **2016**, *49*, 1731–1740. [CrossRef]
7. Zhang, Z.; Du, Y.; Shi, X.; Wang, K.; Qu, Q.; Liang, Q.; Ma, X.; He, K.; Chi, C.; Tang, J.; et al. NIR-II light in clinical oncology: Opportunities and challenges. *Nat. Rev. Clin. Oncol.* **2024**, *21*, 449–467. [CrossRef] [PubMed]
8. Dunn, B.; Hanafi, M.; Hummel, J.; Cressman, J.R.; Veneziano, R.; Chitnis, P.V. NIR-II nanoprobes: A review of components-based approaches to next-generation bioimaging probes. *Bioengineering* **2023**, *10*, 954. [CrossRef]
9. Feng, Z.; Tang, T.; Wu, T.; Yu, X.; Zhang, Y.; Wang, M.; Zheng, J.; Ying, Y.; Chen, S.; Zhou, J.; et al. Perfecting and extending the near-infrared imaging window. *Light Sci. Appl.* **2021**, *10*, 197. [CrossRef]
10. Yang, Y.; Fan, X.; Li, L.; Yang, Y.; Nuernisha, A.; Xue, D.; He, C.; Qian, J.; Hu, Q.; Chen, H.; et al. Semiconducting polymer nanoparticles as theranostic system for near-infrared-II fluorescence imaging and photothermal therapy under safe laser fluence. *ACS Nano* **2020**, *14*, 2509–2521. [CrossRef]
11. Lee, K.W.; Wan, Y.; Huang, Z.; Zhao, Q.; Li, S.; Lee, C.S. Organic Optoelectronic Materials: A Rising star of bioimaging and phototherapy. *Adv. Mater.* **2024**, *36*, e2306492. [CrossRef] [PubMed]
12. Ma, D.; Bian, H.; Gu, M.; Wang, L.; Chen, X.; Peng, X. Recent advances in the design and applications of near-infrared II responsive small molecule phototherapeutic agents. *Coord. Chem. Rev.* **2024**, *505*, 215677. [CrossRef]
13. Jiang, Z.; Ding, Y.; Lovell, J.F.; Zhang, Y. Design and application of organic contrast agents for molecular imaging in the second near infrared (NIR-II) window. *Photoacoustics* **2022**, *28*, 100426. [CrossRef]
14. Wan, Y.; Gao, Y.; Wei, W.C.; Lee, K.W.; Tan, J.H.; Chen, C.Y.; Chen, H.; Li, S.; Wong, K.T.; Lee, C.S. Facilely achieving near-infrared-II J-aggregates through molecular bending on a donor-acceptor fluorophore for high-performance tumor phototheranostics. *ACS Nano* **2024**, *18*, 27949–27961. [CrossRef] [PubMed]

15. Heo, J.; Murale, D.P.; Yoon, H.Y.; Arun, V.; Choi, S.; Kim, E.; Lee, J.-S.; Kim, S. Recent trends in molecular aggregates: An exploration of biomedicine. *Aggregate* **2022**, *3*, e159. [CrossRef]
16. Gu, J.; Li, Z.; Li, Q. From single molecule to molecular aggregation science. *Coord. Chem. Rev.* **2023**, *475*, 214872. [CrossRef]
17. Hu, X.; Zhu, C.; Sun, F.; Chen, Z.; Zou, J.; Chen, X.; Yang, Z. J-aggregation strategy toward potentiated NIR-II fluorescence bioimaging of molecular fluorophores. *Adv. Mater.* **2024**, *36*, e2304848. [CrossRef]
18. Deng, Y.; Yuan, W.; Jia, Z.; Liu, G. H- and J-aggregation of fluorene-based chromophores. *J. Phys. Chem. B* **2014**, *118*, 14536–14545. [CrossRef] [PubMed]
19. Peng, Q.; Shuai, Z. Molecular mechanism of aggregation-induced emission. *Aggregate* **2021**, *2*, e91. [CrossRef]
20. Ma, S.; Du, S.; Pan, G.; Dai, S.; Xu, B.; Tian, W. Organic molecular aggregates: From aggregation structure to emission property. *Aggregate* **2021**, *2*, e96. [CrossRef]
21. Liu, Y.; Song, Y.; Zhu, Z.-H.; Ji, C.; Li, J.; Jia, H.; Shi, Y.; Hu, F.; Zhao, Z.; Ding, D.; et al. Twisted-planar molecular engineering with sonication-induced J-aggregation to design near-infrared j-aggregates for enhanced phototherapy. *Angew. Chem. Int. Ed.* **2024**, *64*, e202419428. [CrossRef]
22. Li, Z.; Liang, P.-Z.; Xu, L.; Zhang, X.-X.; Li, K.; Wu, Q.; Lou, X.-F.; Ren, T.-B.; Yuan, L.; Zhang, X.-B. In situ orderly self-assembly strategy affording NIR-II-J-aggregates for in vivo imaging and surgical navigation. *Nat. Commun.* **2023**, *14*, 1843. [CrossRef]
23. Wu, S.; Zhang, W.; Li, C.; Ni, Z.; Chen, W.; Gai, L.; Tian, J.; Guo, Z.; Lu, H. Rational design of CT-coupled J-aggregation platform based on Aza-BODIPY for highly efficient phototherapy. *Chem. Sci.* **2024**, *15*, 5973–5979. [CrossRef] [PubMed]
24. Witte, F.; Rietsch, P.; Sinha, S.; Krappe, A.; Joswig, J.O.; Götze, J.P.; Nirmalananthan-Budau, N.; Resch-Genger, U.; Eigler, S.; Paulus, B. Fluorescence quenching in J-aggregates through the formation of unusual metastable dimers. *J. Phys. Chem. B* **2021**, *125*, 4438–4446. [CrossRef]
25. Tang, F.; Yu, H.; Huang, Y.; Zhao, X.; Chen, Z.; Ma, H.; Zheng, B.-Y.; Ke, M.-R.; Zhang, Y.; Li, X.; et al. Phthalocyanine J-aggregate nanoparticles with enormous-redshifted and intense absorption: Potential structure-J-aggregation relationships and application in tumor-associated macrophages-targeted phototheranostics. *Chem. Eng. J.* **2024**, *496*, 154272. [CrossRef]
26. Wang, X.; Jiang, Z.; Liang, Z.; Wang, T.; Chen, Y.; Liu, Z. Discovery of BODIPY J-aggregates with absorption maxima beyond 1200 nm for biophotonics. *Sci. Adv.* **2022**, *8*, eadd5660. [CrossRef]
27. Qiao, W.; Ma, T.; Xie, G.; Xu, J.; Yang, Z.R.; Zhong, C.; Jiang, H.; Xia, J.; Zhang, L.; Zhu, J.; et al. Supramolecular H-aggregates of squaraines with enhanced type I photosensitization for combined photodynamic and photothermal therapy. *ACS Nano* **2024**, *18*, 25671–25684. [CrossRef]
28. Wu, F.; Lu, Y.; Mu, X.; Chen, Z.; Liu, S.; Zhou, X.; Liu, S.; Li, Z. Intriguing H-aggregates of heptamethine cyanine for imaging-guided photothermal cancer therapy. *ACS Appl. Mater. Interfaces* **2020**, *12*, 32388–32396. [CrossRef] [PubMed]
29. Xu, J.; Yin, Z.; Zhang, L.; Dong, Q.; Cai, X.; Li, S.; Chen, Q.; Keoingthong, P.; Li, Z.; Chen, L.; et al. Hydrogen-bonding-induced h-aggregation of charge-transfer complexes for ultra-efficient second near-infrared region photothermal conversion. *CCS Chem.* **2022**, *4*, 2333–2343.
30. Li, X.; Yang, M.; Cao, J.; Gu, H.; Liu, W.; Xia, T.; Sun, W.; Fan, J.; Peng, X. H-aggregates of prodrug-hemicyanine conjugate for enhanced photothermal therapy and sequential hypoxia-activatedchemotherapy. *ACS Mater. Lett.* **2022**, *4*, 724–732. [CrossRef]
31. Zhang, N.; Liu, L.; Chang, H.; Liu, K.; Liu, T.; Ding, L.; Fang, Y. Tunable non-Kasha behaviors and excited-state dynamics of quadrupolar squaraine aggregates. *J. Phys. Chem. Lett.* **2023**, *14*, 7283–7289. [CrossRef]
32. Hinton, D.A.; Ng, J.D.; Sun, J.; Lee, S.; Saikin, S.K.; Logsdon, J.; White, D.S.; Marquard, A.N.; Cavell, A.C.; Krasecki, V.K.; et al. Mapping forbidden emission to structure in self-assembled organic nanoparticles. *J. Am. Chem. Soc.* **2018**, *140*, 15827–15841. [CrossRef]
33. Ryu, N.; Okazaki, Y.; Pouget, E.; Takafuji, M.; Nagaoka, S.; Ihara, H.; Oda, R. Fluorescence emission originated from the H-aggregated cyanine dye with chiral gemini surfactant assemblies having a narrow absorption band and a remarkably large Stokes shift. *Chem. Comm.* **2017**, *53*, 8870–8873. [CrossRef]
34. Dixit, S.J.N.; Ghosh, R.; Agarwal, N. Unveiling emissive H-aggregates of benzocoronenediimide, their photophysics and ultrafast exciton dynamics. *Phys. Chem. Chem. Phys.* **2025**, *27*, 175–181. [CrossRef]
35. Zhang, H.; Zhao, Z.; Turley, A.T.; Wang, L.; McGonigal, P.R.; Tu, Y.; Li, Y.; Wang, Z.; Kwok, R.T.K.; Lam, J.W.Y.; et al. Aggregate science: From structures to properties. *Adv. Mater.* **2020**, *32*, 2001457. [CrossRef] [PubMed]
36. Cai, X.; Liu, B. Aggregation-induced emission: Recent advances in materials and biomedical applications. *Angew. Chem. Int. Ed.* **2020**, *59*, 9868–9886. [CrossRef]
37. Wang, D.; Su, H.; Kwok, R.T.K.; Hu, X.; Zou, H.; Luo, Q.; Lee, M.M.S.; Xu, W.; Lam, J.W.Y.; Tang, B.Z. Rational design of a water-soluble NIR AIEgen, and its application in ultrafast wash-free cellular imaging and photodynamic cancer cell ablation. *Chem. Sci.* **2018**, *9*, 3685–3693. [CrossRef] [PubMed]
38. Hong, G.; Zou, Y.; Antaris, A.L.; Diao, S.; Wu, D.; Cheng, K.; Zhang, X.; Chen, C.; Liu, B.; He, Y.; et al. Ultrafast fluorescence imaging in vivo with conjugated polymer fluorophores in the second near-infrared window. *Nat. Commun.* **2014**, *5*, 4206. [CrossRef] [PubMed]

39. Mu, J.; Xiao, M.; Shi, Y.; Geng, X.; Li, H.; Yin, Y.; Chen, X. The chemistry of organic contrast agents in the NIR-II window. *Angew. Chem. Int. Ed.* **2022**, *61*, e202114722. [CrossRef]
40. Li, B.; Lu, L.; Zhao, M.; Lei, Z.; Zhang, F. An efficient 1064 nm NIR-II excitation fluorescent molecular dye for deep-tissue high-resolution dynamic bioimaging. *Angew. Chem. Int. Ed.* **2018**, *57*, 7483–7487. [CrossRef]
41. Shi, Y.; Yuan, W.; Liu, Q.; Kong, M.; Li, Z.; Feng, W.; Hu, K.; Li, F. Development of polyene-bridged hybrid rhodamine fluorophores for high-resolution NIR-II imaging. *ACS Mater. Lett.* **2019**, *1*, 418–424. [CrossRef]
42. Bai, L.; Sun, P.; Liu, Y.; Zhang, H.; Hu, W.; Zhang, W.; Liu, Z.; Fan, Q.; Li, L.; Huang, W. Novel aza-BODIPY based small molecular NIR-II fluorophores for in vivo imaging. *Chem. Commun.* **2019**, *55*, 10920–10923. [CrossRef]
43. Carr, J.A.; Franke, D.; Caram, J.R.; Perkinson, C.F.; Saif, M.; Askoxylakis, V.; Datta, M.; Fukumura, D.; Jain, R.K.; Bawendi, M.G.; et al. Shortwave infrared fluorescence imaging with the clinically approved near-infrared dye indocyanine green. *Proc. Natl. Acad. Sci. USA* **2018**, *115*, 4465–4470. [CrossRef] [PubMed]
44. Starosolski, Z.; Bhavane, R.; Ghaghada, K.B.; Vasudevan, S.A.; Kaay, A.; Annapragada, A. Indocyanine green fluorescence in second near-infrared (NIR-II) window. *PLoS ONE* **2017**, *12*, e0187563. [CrossRef] [PubMed]
45. Hu, Z.; Fang, C.; Li, B.; Zhang, Z.; Cao, C.; Cai, M.; Su, S.; Sun, X.; Shi, X.; Li, C.; et al. First-in-human liver-tumour surgery guided by multispectral fluorescence imaging in the visible and near-infrared-I/II windows. *Nat. Biomed. Eng.* **2020**, *4*, 259–271. [CrossRef]
46. Li, K.; Duan, X.; Jiang, Z.; Ding, D.; Chen, Y.; Zhang, G.Q.; Liu, Z. J-aggregates of meso-[2.2]paracyclophanyl-BODIPY dye for NIR-II imaging. *Nat. Commun.* **2021**, *12*, 2376. [CrossRef]
47. Sun, C.; Li, B.; Zhao, M.; Wang, S.; Lei, Z.; Lu, L.; Zhang, H.; Feng, L.; Dou, C.; Yin, D.; et al. J-aggregates of cyanine dye for NIR-II in vivo dynamic vascular imaging beyond 1500 nm. *J. Am. Chem. Soc.* **2019**, *141*, 19221–19225. [CrossRef]
48. Jelley, E.E. Spectral absorption and fluorescence of dyes in the molecular state. *Nature* **1936**, *138*, 1009–1010. [CrossRef]
49. Scheibe, G. Auxiliary valency as the cause of variability in the absorption spectra in solutions. *Angew. Chem. Int. Ed.* **1937**, *50*, 0212–0219. [CrossRef]
50. Kopainsky, B.; Hallermeier, J.K.; Kaiser, W. The first step of aggregation of pic: The dimerization. *Chem. Phys. Lett.* **1981**, *83*, 498–502. [CrossRef]
51. Wuerthner, F.; Kaiser, T.E.; Saha-Moeller, C.R. J-aggregates: From serendipitous discovery to supramolecular engineering of functional dye materials. *Angew. Chem. Int. Ed.* **2011**, *50*, 3376–3410. [CrossRef] [PubMed]
52. Mobius, D. Scheibe aggregates. *Adv. Mater.* **1995**, *7*, 437–444. [CrossRef]
53. Czlikkely, V.; Foersterling, H.D.; Kuhn, H. Light absorption and structure of aggregates of dye molecules. *Chem. Phys. Lett.* **1970**, *6*, 11–14. [CrossRef]
54. Kasha, M.; Rawls, H.R.; El-Bayoumi, M.A. The exciton model in molecular spectroscopy. *Pure Appl. Chem.* **1965**, *11*, 371–392.
55. Darghouth, A.; Correa, G.C.; Juillard, S.; Casida, M.E.; Humeniuk, A.; Mitrić, R. Davydov-type excitonic effects on the absorption spectra of parallel-stacked and herringbone aggregates of pentacene: Time-dependent density-functional theory and time-dependent density-functional tight binding. *J. Chem. Phys.* **2018**, *149*, 134111. [CrossRef] [PubMed]
56. Xue, J.; Liang, Q.; Wang, R.; Hou, J.; Li, W.; Peng, Q.; Shuai, Z.; Qiao, J. Highly efficient thermally activated delayed fluorescence via J-aggregates with strong intermolecular charge transfer. *Adv. Mater.* **2019**, *31*, e1808242. [CrossRef]
57. Scheibe, G. Reversible polymerisation als ursache neuartiger absorptionsbanden von farbstoffen. *Kolloid-Zeitschrift* **1938**, *82*, 1–14. [CrossRef]
58. Hestand, N.J.; Spano, F.C. Molecular aggregate photophysics beyond the Kasha model: Novel design principles for organic materials. *Acc. Chem. Res.* **2017**, *50*, 341–350. [CrossRef]
59. Kim, J.H.; Schembri, T.; Bialas, D.; Stolte, M.; Würthner, F. Slip-stacked J-aggregate materials for organic solar cells and photodetectors. *Adv. Mater.* **2022**, *34*, e2104678. [CrossRef] [PubMed]
60. Dexter, D.L. A theory of sensitized luminescence in solids. *J. Chem. Phys.* **1953**, *21*, 836–850. [CrossRef]
61. Harcourt, R.D.; Ghiggino, K.P.; Scholes, G.D.; Speiser, S. On the origin of matrix elements for electronic excitation (energy) transfer. *J. Chem. Phys.* **1996**, *105*, 1897–1901. [CrossRef]
62. Zhao, L.; Ren, X.; Yan, X. Assembly induced super-large red-shifted absorption: The burgeoning field of organic near-infrared materials. *CCS Chem.* **2021**, *3*, 678–693. [CrossRef]
63. Bricks, J.L.; Slominskii, Y.L.; Panas, I.D.; Demchenko, A.P. Fluorescent J-aggregates of cyanine dyes: Basic research and applications review. *Methods Appl. Fluoresc.* **2017**, *6*, 012001. [CrossRef]
64. Yuan, J.; Wang, S.; Ji, Y.; Chen, R.; Zhu, Q.; Wang, Y.; Zheng, C.; Tao, Y.; Fan, Q.; Huang, W. Invoking ultralong room temperature phosphorescence of purely organic compounds through H-aggregation engineering. *Mater. Horiz.* **2019**, *6*, 1259–1264. [CrossRef]
65. Rösch, U.; Yao, S.; Wortmann, R.; Würthner, F. Fluorescent H-aggregates of merocyanine dyes. *Angew. Chem. Int. Ed.* **2006**, *45*, 7026–7030. [CrossRef] [PubMed]

66. Basak, S.; Nandi, N.; Bhattacharyya, K.; Datta, A.; Banerjee, A. Fluorescence from an H-aggregated naphthalenediimide based peptide: Photophysical and computational investigation of this rare phenomenon. *Phys. Chem. Chem. Phys.* **2015**, *17*, 30398–30403. [CrossRef]
67. Reddy, N.R.; Aubin, M.; Kushima, A.; Fang, J. Fluorescent H-aggregate vesicles and tubes of a cyanine dye and their potential as light-harvesting antennae. *J. Phys. Chem. B* **2021**, *125*, 7911–7918. [CrossRef] [PubMed]
68. Luo, J.; Xie, Z.; Lam, J.W.; Cheng, L.; Chen, H.; Qiu, C.; Kwok, H.S.; Zhan, X.; Liu, Y.; Zhu, D.; et al. Aggregation-induced emission of 1-methyl-1,2,3,4,5-pentaphenylsilole. *Chem. Commun.* **2001**, *18*, 1740–1741. [CrossRef]
69. Stokes, G.G. On the change of refrangibility of light. *Philos. Trans.* **1854**, *142*, 463.
70. Mei, J.; Leung, N.L.; Kwok, R.T.; Lam, J.W.; Tang, B.Z. Aggregation-induced emission: Together we shine, united we soar! *Chem. Rev.* **2015**, *115*, 11718–11940. [CrossRef]
71. Yin, S.; Peng, Q.; Shuai, Z.; Fang, W.; Wang, Y.-H.; Luo, Y. Aggregation-enhanced luminescence and vibronic coupling of silole molecules from first principles. *Phys. Rev. B* **2006**, *73*, 205409. [CrossRef]
72. Cheng, Y.; Dai, J.; Sun, C.; Liu, R.; Zhai, T.; Lou, X.; Xia, F. An intracellular H_2O_2-responsive aiegen for the peroxidase-mediated selective imaging and inhibition of inflammatory cells. *Angew. Chem. Int. Ed.* **2018**, *57*, 3123–3127. [CrossRef]
73. Zhang, C.; Wu, Y.; Zeng, F.; Wen, Y.; Chen, J.; Deng, G.; Zhang, L.; Zhao, S.; Wu, S.; Zhao, Y. Structurally modulated formation of cyanine J-aggregates with sharp and tunable spectra for multiplexed optoacoustic and fluorescence bioimaging. *Angew. Chem. Int. Ed.* **2024**, *63*, e202406694. [CrossRef] [PubMed]
74. Bao, X.; Zheng, S.; Zhang, L.; Shen, A.; Zhang, G.; Liu, S.; Hu, J. Nitric-oxide-releasing aza-BODIPY: A new near-infrared J-aggregate with multiple antibacterial modalities. *Angew. Chem. Int. Ed.* **2022**, *61*, e202207250. [CrossRef]
75. Ogawa, M.; Kosaka, N.; Choyke, P.L.; Kobayashi, H. H-type dimer formation of fluorophores: A mechanism for activatable, in vivo optical molecular imaging. *ACS Chem. Biol.* **2009**, *4*, 535–546. [CrossRef]
76. Wei, K.; Wu, Y.; Li, P.; Zheng, X.; Ji, C.; Yin, M. Modulating planarity of cyanine dye to construct highly stable H-aggregates for enhanced photothermal therapy. *Nano Res.* **2023**, *16*, 970–979. [CrossRef]
77. Li, Y.; Cai, Z.; Liu, S.; Zhang, H.; Wong, S.T.H.; Lam, J.W.Y.; Kwok, R.T.K.; Qian, J.; Tang, B.Z. Design of AIEgens for near-infrared IIb imaging through structural modulation at molecular and morphological levels. *Nat. Commun.* **2020**, *11*, 1255. [CrossRef] [PubMed]
78. Shen, H.; Sun, F.; Zhu, X.; Zhang, J.; Ou, X.; Zhang, J.; Xu, C.; Sung, H.H.Y.; Williams, I.D.; Chen, S.; et al. Rational design of NIR-II AIEgens with ultrahigh quantum yields for photo- and chemiluminescence imaging. *J. Am. Chem. Soc.* **2022**, *144*, 15391–15402. [CrossRef]
79. Yan, D.; Zhang, Z.; Zhang, J.; Li, X.; Wu, Q.; Gui, Y.; Zhu, J.; Kang, M.; Chen, X.; Tang, B.Z.; et al. An all-rounder for NIR-II phototheranostics: Well-tailored 1064 nm-excitable molecule for photothermal combating of orthotopic breast cancer. *Angew. Chem. Int. Ed.* **2024**, *63*, e202401877. [CrossRef]
80. Li, B.; Wang, W.; Zhao, L.; Wu, Y.; Li, X.; Yan, D.; Gao, Q.; Yan, Y.; Zhang, J.; Feng, Y.; et al. Photothermal therapy of tuberculosis using targeting pre-activated macrophage membrane-coated nanoparticles. *Nat. Nanotechnol.* **2024**, *19*, 834–845. [CrossRef]
81. Cai, K.; Xie, J.; Zhang, D.; Shi, W.; Yan, Q.; Zhao, D. Concurrent cooperative J-aggregates and anticooperative H-aggregates. *J. Am. Chem. Soc.* **2018**, *140*, 5764–5773. [CrossRef] [PubMed]
82. Harmatys, K.M.; Chen, J.; Charron, D.M.; MacLaughlin, C.M.; Zheng, G. Multipronged biomimetic approach to create optically tunable nanoparticles. *Angew. Chem. Int. Ed.* **2018**, *57*, 8125–8129. [CrossRef] [PubMed]
83. Cheng, M.H.Y.; Harmatys, K.M.; Charron, D.M.; Chen, J.; Zheng, G. Stable J-aggregation of an aza-BODIPY-lipid in a liposome for optical cancer imaging. *Angew. Chem. Int. Ed.* **2019**, *58*, 13394–13399. [CrossRef]
84. Hou, W.; Lou, J.W.H.; Bu, J.; Chang, E.; Ding, L.; Valic, M.; Jeon, H.H.; Charron, D.M.; Coolens, C.; Cui, D.; et al. A nanoemulsion with a porphyrin shell for cancer theranostics. *Angew. Chem. Int. Ed.* **2019**, *58*, 14974–14978. [CrossRef] [PubMed]
85. Liu, Y.; Yang, G.; Jin, S.; Zhang, R.; Chen, P.; Tengjisi; Wang, L.; Chen, D.; Weitz, D.A.; Zhao, C.X. J-Aggregate-based FRET monitoring of drug release from polymer nanoparticles with high drug loading. *Angew. Chem. Int. Ed.* **2020**, *59*, 20065–20074. [CrossRef] [PubMed]
86. Zhang, Q.; Yu, P.; Fan, Y.; Sun, C.; He, H.; Liu, X.; Lu, L.; Zhao, M.; Zhang, H.; Zhang, F. Bright and stable NIR-II J-aggregated aie dibodipy-based fluorescent probe for dynamic in vivo bioimaging. *Angew. Chem. Int. Ed.* **2021**, *60*, 3967–3973. [CrossRef]
87. Kim, T.I.; Hwang, B.; Lee, B.; Bae, J.; Kim, Y. Selective monitoring and imaging of eosinophil peroxidase activity with a J-aggregating probe. *J. Am. Chem. Soc.* **2018**, *140*, 11771–11776. [CrossRef] [PubMed]
88. Chen, W.; Cheng, C.A.; Cosco, E.D.; Ramakrishnan, S.; Lingg, J.G.P.; Bruns, O.T.; Zink, J.I.; Sletten, E.M. Shortwave infrared imaging with J-aggregates stabilized in hollow mesoporous silica nanoparticles. *J. Am. Chem. Soc.* **2019**, *141*, 12475–12480. [CrossRef] [PubMed]
89. Wood, C.A.; Han, S.; Kim, C.S.; Wen, Y.; Sampaio, D.R.T.; Harris, J.T.; Homan, K.A.; Swain, J.L.; Emelianov, S.Y.; Sood, A.K.; et al. Clinically translatable quantitative molecular photoacoustic imaging with liposome-encapsulated ICG J-aggregates. *Nat. Commun.* **2021**, *12*, 5410. [CrossRef]

90. Lin, H.; Zhou, Y.; Wang, J.; Wang, H.; Yao, T.; Chen, H.; Zheng, H.; Zhang, Y.; Ren, E.; Jiang, L.; et al. Repurposing ICG enables MR/PA imaging signal amplification and iron depletion for iron-overload disorders. *Sci. Adv.* **2021**, *7*, eabl5862. [CrossRef] [PubMed]
91. Li, Z.; Liang, P.Z.; Ren, T.B.; Yuan, L.; Zhang, X.B. Orderly self-assembly of organic fluorophores for sensing and imaging. *Angew. Chem. Int. Ed.* **2023**, *62*, e202305742. [CrossRef] [PubMed]
92. Bouit, P.A.; Aronica, C.; Toupet, L.; Le Guennic, B.; Andraud, C.; Maury, O. Continuous symmetry breaking induced by ion pairing effect in heptamethine cyanine dyes: Beyond the cyanine limit. *J. Am. Chem. Soc.* **2010**, *132*, 4328–4335. [CrossRef] [PubMed]
93. Li, Y.; Ma, T.; Jiang, H.; Li, W.; Tian, D.; Zhu, J.; Li, Z. Anionic cyanine J-type aggregate nanoparticles with enhanced photosensitization for mitochondria-targeting tumor phototherapy. *Angew. Chem. Int. Ed.* **2022**, *61*, e202203093. [CrossRef] [PubMed]
94. Ma, X.; Huang, Y.; Chen, W.; Liu, J.; Liu, S.H.; Yin, J.; Yang, G.F. J-aggregates formed by NaCl treatment of aza-coating heptamethine cyanines and their application to monitoring salt stress of plants and promoting photothermal therapy of tumors. *Angew. Chem. Int. Ed.* **2023**, *62*, e202216109. [CrossRef] [PubMed]
95. Lee, K.W.; Gao, Y.; Wei, W.C.; Tan, J.H.; Wan, Y.; Feng, Z.; Zhang, Y.; Liu, Y.; Zheng, X.; Cao, C.; et al. Anti-quenching NIR-II J-aggregates of Benzo[c]thiophene fluorophore for highly efficient bioimaging and phototheranostics. *Adv. Mater.* **2023**, *35*, e2211632. [CrossRef] [PubMed]
96. Su, M.; Li, S.; Zhang, H.; Zhang, J.; Chen, H.; Li, C. Nano-assemblies from J-aggregated dyes: A stimuli-responsive tool applicable to living systems. *J. Am. Chem. Soc.* **2019**, *141*, 402–413. [CrossRef] [PubMed]
97. Zhao, F.; Zhang, X.; Bai, F.; Lei, S.; He, G.; Huang, P.; Lin, J. Maximum emission peak over 1500 nm of organic assembly for blood-brain barrier-crossing NIR-IIb phototheranostics of orthotopic glioblastoma. *Adv. Mater.* **2023**, *35*, e2208097. [CrossRef] [PubMed]
98. Guo, X.; Yang, J.; Li, M.; Zhang, F.; Bu, W.; Li, H.; Wu, Q.; Yin, D.; Jiao, L.; Hao, E. Unique double intramolecular and intermolecular exciton coupling in ethene-bridged aza-BODIPY dimers for high-efficiency near-infrared photothermal conversion and therapy. *Angew. Chem. Int. Ed.* **2022**, *61*, e202211081. [CrossRef]
99. Zhang, Z.; Kang, M.; Tan, H.; Song, N.; Li, M.; Xiao, P.; Yan, D.; Zhang, L.; Wang, D.; Tang, B.Z. The fast-growing field of photo-driven theranostics based on aggregation-induced emission. *Chem. Soc. Rev.* **2022**, *51*, 1983–2030. [CrossRef]
100. Wu, K.; Liu, J.; Zhang, X.; Chao, Z.; Fang, Y.; Zhu, Y.; Liu, Y.; Zhang, X.; Wang, Q.; Ju, H.; et al. Bovine serum albumin framed activatable NIR AIE photosensitizer for targeted tumor therapy. *Biomaterials* **2025**, *315*, 122918. [CrossRef]